J. Fluid Mech. (2016), *vol.* 799, *pp.* 159–199. © Cambridge University Press 2016
doi:10.1017/jfm.2016.362

Spectral modelling for passive scalar dynamics in homogeneous anisotropic turbulence

A. Briard[1], T. Gomez[2,3,†] and C. Cambon[4]

[1]∂'Alembert, CNRS UMR 7190, 4 Place Jussieu, 75252 Paris CEDEX 5, France
[2]USTL, LML, 59650 Villeneuve d'Ascq, France
[3]Université Lille Nord de France, F-59000 Lille, France
[4]Laboratoire de Mécanique des Fluides et d'Acoustique, Ecole Centrale de Lyon, 69134 Écully, France

(Received 6 January 2016; revised 13 May 2016; accepted 25 May 2016;
first published online 22 June 2016)

The present work aims at developing a spectral model for a passive scalar field and its associated scalar flux in homogeneous anisotropic turbulence. This is achieved using the paradigm of eddy-damped quasi-normal Markovian (EDQNM) closure extended to anisotropic flows. In order to assess the validity of this approach, the model is compared to several detailed direct numerical simulations (DNS) and experiments of shear-driven flows and isotropic turbulence with a mean scalar gradient at moderate Reynolds numbers. This anisotropic modelling is then used to investigate the passive scalar dynamics at very high Reynolds numbers. In the framework of homogeneous isotropic turbulence submitted to a mean scalar gradient, decay and growth exponents for the cospectrum and scalar energies are obtained analytically and assessed numerically thanks to EDQNM closure. With the additional presence of a mean shear, the scaling of the scalar flux and passive scalar spectra in the inertial range are investigated and confirm recent theoretical predictions. Finally, it is found that, in shear-driven flows, the small scales of the scalar second-order moments progressively return to isotropy when the Reynolds number increases.

Key words: homogeneous turbulence, turbulence modelling, turbulent mixing

1. Introduction

The study of a passive scalar, such as small temperature fluctuations θ, convected by a turbulent velocity field u_i is of interest for several reasons. From a fundamental point of view, though homogeneous anisotropic turbulence (HAT) has been at the centre of many theoretical, numerical and experimental works for almost 40 years, numerous questions still remain without clear answers. How does the energy, mainly produced at large scales by mean velocity and scalar gradients, affect the small-scale dynamics? Is there a complete return to isotropy of small scales? Is the growth or decay dynamics of quantities, such as the kinetic energy and the scalar variance, predictable?

Upstream to these fundamental questions, there are practical reasons for the investigation of HAT. Indeed, taking into account anisotropy created by non-zero mean

† Email address for correspondence: thomas.gomez@univ-lille1.fr

fields is an important feature to describe real flows by comparison to the classical case of homogeneous and isotropic turbulence (HIT). Notably, the deep understanding of homogeneous turbulence dynamics could provide further insights into the analysis of high-Reynolds-number natural flows such as atmospheric and oceanic ones. Such flows are complex for multiple reasons, one being that their Reynolds numbers are much higher than the ones currently reachable in direct numerical simulations (DNS) and experiments. For instance, the Reynolds number based on the Taylor micro-scale $Re_\lambda = K\sqrt{20/3\nu\epsilon}$ (where $K = \langle u_i u_i \rangle/2$ is the kinetic energy, $\epsilon = \nu\langle \partial_j u_i \partial_j u_i \rangle$ its dissipation rate, u_i the fluctuating velocity, and ν the kinematic viscosity) can be of the order of 10^4 in atmospheric flows. Such large-Reynolds-number simulations without modelling would require huge computational resources to capture only the early stage of the dynamics, and would need a fine description of all scales, from the most energetic ones to the dissipative ones at the level of the Kolmogorov scale $\eta = (\epsilon/\nu^3)^{-1/4}$. In addition to very high Reynolds numbers involved in atmospheric flows, the nature itself of such flows is complex, as it contains many different physical phenomena. Indeed, a fine description of atmospheric dynamics would require account to be taken of rotation, helicity, stratification, shear and mean scalar gradient from the ground to high altitude (Wyngaard & Coté 1972; Kader & Yaglom 1991). Mean velocity and scalar gradients are also deeply associated with production mechanisms in the turbulence dynamics regardless of the flow type. Indeed, they play a fundamental role in the energy transfers through scales. Therefore, insights concerning the role of mean velocity or scalar gradients are of great interest for turbulent flows, and specifically the ones where departure from isotropy is generated by anisotropic forces or by solid walls giving rise to shearing stresses. Moreover, a better understanding of all these anisotropic turbulent flows could be obtained by making separate investigations of isolated mechanisms at high Reynolds numbers, which are still quite unreachable using DNS.

This is the approach followed in this study. In order to achieve this objective, notably for very high Reynolds numbers, the dynamics of a passive scalar field θ and its flux $\langle u_i\theta \rangle$ in HAT is addressed with the use of an eddy-damped quasi-normal Markovian (EDQNM) closure adapted to anisotropic flows. The modelling proposed here is an extension to the scalar case of a model recently developed by Mons, Cambon & Sagaut (2016). The purpose of this work is therefore twofold: developing the theoretical basis of an anisotropic EDQNM modelling for the passive scalar, and using it to investigate non-helical high-Reynolds-number turbulence. Moreover, the present model is developed for arbitrary mean velocity gradients that produce energy: consequently, it is not adapted to the case of purely rotating turbulence in which there is no energy production and where the dynamics is dominated by dispersive (inertial) waves interacting nonlinearly, requiring even more complex tools (Cambon & Jacquin 1989; Sagaut & Cambon 2008). The emphasis is thus put on three different configurations: homogeneous isotropic turbulence with a mean scalar gradient (HITSG), homogeneous shear turbulence (HST), and finally these two frameworks combined into homogeneous shear turbulence with mean scalar gradient (HSTSG) as notably encountered in atmospheric flows.

In HITSG, the mean scalar gradient $\Lambda = \mathrm{d}\Theta/\mathrm{d}x_3$, where Θ is the mean scalar field, produces scalar fluctuations so that the scalar variance $K_T = \langle \theta^2 \rangle$ can increase whereas the isotropic velocity field is decaying. This mean scalar gradient creates an anisotropic flux $\langle u_3\theta \rangle$, called the cospectrum in spectral space, which has received a lot of attention: with spectral closures (Herr, Wang & Collins 1996; O'Gorman & Pullin 2003; Bos *et al.* 2004; Bos, Touil & Bertoglio 2005; O'Gorman & Pullin 2005),

with DNS (Pumir 1994; Overholt & Pope 1996), theoretically (Lumley 1967) and experimentally (Venkataramani & Chevray 1978; Warhaft 1980; Sirivat & Warhaft 1983; Jayesh & Warhaft 1992; Mydlarski & Warhaft 1998; Mydlarski 2003). In all these studies, the scaling of the cospectrum is uncertain in the inertial range, $k^{-7/3}$ or k^{-2}, probably because of too low Reynolds numbers. This point will be addressed hereafter.

The case of a mean velocity gradient $S = \mathrm{d}U_1/\mathrm{d}x_3$, where U_i is the mean velocity field, without mean scalar gradient, has been less studied: a rapid decrease of K_T was observed experimentally (Warhaft 1980; Karnik & Tavoularis 1989), and this has been confirmed theoretically (Gonzalez 2000). Interestingly, in such a configuration, the evolution of the passive scalar field dynamics is completely different from the one of the velocity field.

Finally, when both mean velocity and scalar gradients are applied, there is a continuous production of kinetic energy $K(t)$ that grows exponentially for large dimensionless times St. Consequently, thanks to interactions with the scalar flux, K_T grows exponentially as well. The HSTSG configuration has been at the centre of many works as well: with a classical EDQNM approach (Bos & Bertoglio 2007), with DNS (Shirani, Ferziger & Reynolds 1981; Rogers, Mansour & Reynolds 1989; Brethouwer 2005; Kassinos, Knaepen & Carati 2007) and experimentally (Tavoularis & Corrsin 1981; Danaila *et al.* 1999; Ferchihi & Tavoularis 2002). Even without rotation, the HSTSG configuration remains quite representative of atmospheric flows (Wyngaard & Coté 1972).

Besides, the small-scale return to isotropy (RTI) for each of the three cases presented is of primary importance: indeed, according to Kolmogorov (1941), the small scales of the flow should return to isotropy whatever the large scales are. While the small-scale RTI of second-order moments of the velocity field is well known (Speziale, Sarkar & Gatski 1990; Pumir 1996; Garg & Warhaft 1998; Shen & Warhaft 2000), the case of third-order moments (such as the derivative skewness of the velocity in shear flows) is still an open question. Moreover, it appeared that the scalar case is even more complicated, since the conclusion is not clear regarding second-order moments: departures from isotropy are observed experimentally and numerically at small scales with a mean scalar gradient only, in shear-driven flows, in boundary layers and in jets (Sreenivasan, Antonia & Britz 1979; Sreenivasan & Tavoularis 1980; Sreenivasan 1991; Pumir 1994; Danaila *et al.* 1999). Consequently, and in order to clarify the RTI of the scalar small scales, high-Reynolds-number anisotropic flows will be investigated thanks to the present modelling.

The general method used to develop the present model, briefly called anisotropic EDQNM, is now described. Firstly, the dynamical equations that govern the evolution of the spectral second-order correlations, referred to as Craya equations, are considered. They have an exact part, linear and closed, which corresponds to mean gradient effects. The second part, originating from triple correlation contributions, is explicitly closed with EDQNM. The closure technique for anisotropic flows is discussed in several papers, with a complete survey in Sagaut & Cambon (2008): for the sake of simplicity, explicit effects of mean velocity and scalar gradients are not taken into account in the equations for three-point third-order correlations. Such effects are important only in the case of interacting waves, as in rotating turbulence (Cambon & Jacquin 1989), and can be globally modelled, without altering the structure of the EDQNM model, as in Burlot *et al.* (2015) for unstably stratified turbulence. The latter study shows the strong analogy between shear-driven flows with passive scalar and stratified buoyant flows, in which the buoyancy fluctuation

(density or temperature) is an active scalar. In a second step, a tractable model is obtained in terms of spherically averaged descriptors, so that the state vector depends only on the wavenumber modulus k: the integration on spherical shells is performed analytically. This procedure in two steps generalizes the pioneering work of Cambon, Jeandel & Mathieu (1981) for the velocity field, and consistently extends the recent model by Mons *et al.* (2016) to the scalar and velocity–scalar correlations modelling.

This method is applied to model the dynamics of the scalar field and of the mixed velocity–scalar correlation in HAT. The closure is presented in §§ 2 and 3, along with the main equations and the anisotropic EDQNM modelling: the evolution equations of the passive scalar and the scalar flux constitute one of the main results of this study. Section 4 is devoted to the validation of the present model, where several detailed comparisons with experimental and numerical works are proposed at moderate Reynolds numbers. Then, new numerical and theoretical results at very high Reynolds numbers are presented in § 5. Finally, § 6 is dedicated to the main conclusions of the present work and perspectives.

2. Closed equations for the passive scalar and scalar flux

In this section, incompressible homogeneous turbulence without rotation and helicity is considered. The evolution equations of the spectral kinetic and scalar second-order correlations are derived. Then, the closure method for the nonlinear terms is presented along with the EDQNM approximation. In what follows, time dependence will sometimes be omitted for better readability.

2.1. *Brief overview of the velocity field*

In this section, the main theoretical aspects of Mons *et al.* (2016) are recalled for the sake of clarity and to introduce important notation. The spectral velocity second-order correlation – or spectral Reynolds stress tensor – is defined as

$$\hat{R}_{ij}(\boldsymbol{k}, t)\delta(\boldsymbol{k}-\boldsymbol{p}) = \langle \hat{u}_i^*(\boldsymbol{p}, t)\hat{u}_j(\boldsymbol{k}, t)\rangle, \tag{2.1}$$

where $\langle\cdot\rangle$ is an ensemble average, $(\cdot)^*$ the complex conjugate, $\boldsymbol{k}$ and $\boldsymbol{p}$ are wavevectors of modulus the wavenumbers k and p, $\hat{(\cdot)}$ denotes the Fourier transform and $\hat{u}_i$ is the spectral fluctuating velocity. Finally, $\hat{R}_{ij}$ corresponds to $R_{ij} = \langle u_i u_j\rangle$ in physical space, and its evolution equation in the presence of a mean velocity gradient $A_{ij} = \mathrm{d}U_i/\mathrm{d}x_j$ is called the Craya equation and reads

$$\left(\frac{\partial}{\partial t} - A_{ln}k_l\frac{\partial}{\partial k_n} + 2\nu k^2\right)\hat{R}_{ij}(\boldsymbol{k}) + M_{in}(\boldsymbol{k})\hat{R}_{nj}(\boldsymbol{k}) + M_{jn}(\boldsymbol{k})\hat{R}_{ni}(\boldsymbol{k}) = T_{ij}^{NL}(\boldsymbol{k}), \tag{2.2}$$

where ν is the kinematic viscosity, $M_{ij}(\boldsymbol{k}) = (\delta_{in} - 2\alpha_i\alpha_n)A_{nj}$, with $\alpha_i = k_i/k$, and T_{ij}^{NL} is the total nonlinear transfer, which can be split into a conservative part and a non-conservative one, the latter being linked to slow pressure terms and thus responsible for the RTI mechanism. The kinetic energy and its dissipation rate are defined as

$$K(t) = \frac{R_{ii}(t)}{2} = \int_0^\infty E(k, t)\,\mathrm{d}k, \quad \epsilon(t) = 2\nu\int_0^\infty k^2 E(k, t)\,\mathrm{d}k = \nu\left\langle\frac{\partial u_i}{\partial x_j}\frac{\partial u_i}{\partial x_j}\right\rangle, \tag{2.3a,b}$$

where $E(k,t)$ is the kinetic energy spectrum. In what follows, the $\mathscr{E}$–Z decomposition is used (Cambon & Rubinstein 2006) for a flow without helicity,

$$\hat{R}_{ij}(\boldsymbol{k}) = \underbrace{\frac{E(k)}{4\pi k^2}P_{ij}(\boldsymbol{k})}_{\hat{R}_{ij}^{(iso)}(\boldsymbol{k})} + \underbrace{\left(\mathscr{E}(\boldsymbol{k}) - \frac{E(k)}{4\pi k^2}\right)P_{ij}(\boldsymbol{k})}_{\hat{R}_{ij}^{(dir)}(\boldsymbol{k})} + \underbrace{\mathrm{Re}(Z(\boldsymbol{k})N_i(\boldsymbol{k})N_j(\boldsymbol{k}))}_{\hat{R}_{ij}^{(pol)}(\boldsymbol{k})}, \tag{2.4}$$

where $\mathrm{Re}(\cdot)$ denotes the real part, and $\mathscr{E} - E/(4\pi k^2)$ reflects directional anisotropy, i.e. the difference between the energy in a given direction and the spherical average, and is linked to the kinetic energy spectrum through an integral on a spherical surface S_k of radius k,

$$E(k,t) = \int_{S_k} \mathscr{E}(\boldsymbol{k},t)\,\mathrm{d}^2\boldsymbol{k} = \frac{1}{2}\int_{S_k} \hat{R}_{ii}(\boldsymbol{k},t)\,\mathrm{d}^2\boldsymbol{k}. \tag{2.5}$$

Then, the complex-valued scalar Z is linked to the polarization anisotropy, i.e. the difference in energy between components, and is related to the spectral Reynolds tensor through

$$Z(\boldsymbol{k},t) = \tfrac{1}{2}\hat{R}_{ij}(\boldsymbol{k},t)N_i^*(\boldsymbol{k})N_j^*(\boldsymbol{k}), \tag{2.6}$$

where N_i are helical modes (Cambon & Jacquin 1989; Waleffe 1992) defined as

$$N_j(\boldsymbol{k}) = e_j^{(2)}(\boldsymbol{k}) - \mathrm{i}e_j^{(1)}(\boldsymbol{k}), \quad \boldsymbol{e}^{(1)} = \frac{\boldsymbol{k}\times\boldsymbol{n}}{|\boldsymbol{k}\times\boldsymbol{n}|}, \quad \boldsymbol{e}^{(2)} = \boldsymbol{e}^{(3)}\times\boldsymbol{e}^{(1)}, \quad \boldsymbol{e}^{(3)} = \boldsymbol{\alpha}, \tag{2.7a–d}$$

where $(\boldsymbol{e}^{(1)}, \boldsymbol{e}^{(2)}, \boldsymbol{e}^{(3)})$ is the Craya–Herring orthonormal right-handed frame of reference associated with a privileged direction $\boldsymbol{n}$. The first step of the derivation proposed by Mons *et al.* (2016) consists in using EDQNM to close the generalized transfer terms in the evolution equations of $\mathscr{E}$ and Z, equivalent to (2.2).

The second step starts with the following truncated expansions of the spectral Reynolds stress tensor for $\mathscr{E}$ and Z for moderately anisotropic flows,

$$\mathscr{E}(\boldsymbol{k},t) = \mathscr{E}_0(1 - 15H_{ij}^{(dir)}(k,t)\alpha_i\alpha_j), \tag{2.8}$$

$$Z(\boldsymbol{k},t) = \tfrac{5}{2}\mathscr{E}_0 H_{ij}^{(pol)}(k,t)N_i^*(\boldsymbol{k})N_j^*(\boldsymbol{k}), \tag{2.9}$$

with $\mathscr{E}_0 = E(k,t)/(4\pi k^2)$, and where $H_{ij}^{(dir)}$ and $H_{ij}^{(pol)}$ are deviatoric tensors that describe anisotropy, defined by a spherical integration

$$2E(k,t)H_{ij}^{(dir)}(k,t) = \int_{S_k} \hat{R}_{ij}^{(dir)}(\boldsymbol{k},t)\,\mathrm{d}^2\boldsymbol{k}, \quad 2E(k,t)H_{ij}^{(pol)}(k,t) = \int_{S_k} \hat{R}_{ij}^{(pol)}(\boldsymbol{k},t)\,\mathrm{d}^2\boldsymbol{k}. \tag{2.10a,b}$$

Finally, these truncated expansions allow one to derive evolution equations for the spherically averaged descriptors E, $H_{ij}^{(dir)}$ and $H_{ij}^{(pol)}$ (see table 1). After the spherical integration, the $\boldsymbol{k}$ dependence is transformed into a k one, according to the expansions into spherical harmonics (2.8) and (2.9): these expansions allow part of the angular dependence information to be restored.

$\boldsymbol{k}$-vector descriptors	Spherically averaged descriptors: Isotropy	Directional anisotropy	Polarization anisotropy
$\mathscr{E}(\boldsymbol{k}, t)$	$E(k, t)$	$H_{ij}^{(dir)}(k, t)$	0
$Z(\boldsymbol{k}, t)$	0	0	$H_{ij}^{(pol)}(k, t)$
$\mathscr{E}^T(\boldsymbol{k}, t)$	$E_T(k, t)$	$H_{ij}^{(T)}(k, t)$	0
$F_i(\boldsymbol{k}, t)$	0	0	$E_i^F(k, t)$

TABLE 1. Description of anisotropy at the velocity, passive scalar and scalar flux levels, using $\boldsymbol{k}$-vector descriptors and their corresponding spherically averaged contributions. Here $\mathscr{E}$, Z, $\mathscr{E}^T$ and F_i are defined respectively in (2.5), (2.6), (2.15) and (2.20).

2.2. *Towards the passive scalar and scalar flux Craya equations*

In order to derive the spectral evolution equations of the scalar–scalar and velocity–scalar second-order correlations, the procedure described in the previous section for obtaining the Craya equation is used. The scalar field T is decomposed into mean and fluctuating parts $T = \Theta + \theta$, with $\langle\theta\rangle = 0$, and the mean scalar gradient is written

$$\lambda_i = \frac{\partial \Theta}{\partial x_i}, \tag{2.11}$$

so that $\Theta = \lambda_i x_i$. In physical space, the evolution equation of the scalar fluctuation θ in the homogeneous framework is

$$\frac{\partial \theta}{\partial t} + A_{jl} x_l \frac{\partial \theta}{\partial x_j} + u_j \lambda_j + \frac{\partial}{\partial x_j}(\theta u_j) = a \frac{\partial^2 \theta}{\partial x_l \partial x_l}, \tag{2.12}$$

where a is the scalar diffusivity. The Fourier transform of the previous equation yields

$$\left(\frac{\partial}{\partial t} - A_{jl} k_j \frac{\partial}{\partial k_l} + a k^2 \right) \hat{\theta} + \lambda_j \hat{u}_j = -\mathrm{i} k_j \widehat{\theta u_j}, \tag{2.13}$$

with the convolution product

$$\widehat{\theta u_j}(\boldsymbol{k}, t) = \int_{\boldsymbol{k}=\boldsymbol{p}+\boldsymbol{q}} \hat{\theta}(\boldsymbol{p}, t) \hat{u}_j(\boldsymbol{q}, t)\, \mathrm{d}^3\boldsymbol{p}. \tag{2.14}$$

Then, the spectral scalar–scalar correlation $\mathscr{E}^T$ is defined as

$$\langle \hat{\theta}^*(\boldsymbol{p}) \hat{\theta}(\boldsymbol{k}) \rangle = \mathscr{E}^T(\boldsymbol{k}) \delta(\boldsymbol{k} - \boldsymbol{p}), \tag{2.15}$$

which corresponds to the second-order correlation $K_T = \langle\theta^2\rangle$ in physical space. Correlation $\mathscr{E}^T$ is real and thus satisfies $\mathscr{E}^T(\boldsymbol{k}) = \mathscr{E}^T(-\boldsymbol{k})$ due to Hermitian symmetry. It is linked to the scalar variance spectrum $E_T(k, t)$ through a spherical integral

$$E_T(k, t) = \int_{S_k} \mathscr{E}^T(\boldsymbol{k}, t)\, \mathrm{d}^2\boldsymbol{k}. \tag{2.16}$$

The Craya equation for the three-dimensional scalar variance spectrum is then

$$\left(\frac{\partial}{\partial t} - A_{jl} k_j \frac{\partial}{\partial k_l} + 2 a k^2 \right) \mathscr{E}^T(\boldsymbol{k}, t) + 2 \lambda_j F_j(\boldsymbol{k}, t) = T^{T,NL}(\boldsymbol{k}, t), \tag{2.17}$$

where $T^{T,NL}$ is the total nonlinear scalar transfer, which can be written

$$T^{T,NL}(\boldsymbol{k},t) = 2k_i \,\mathrm{Re}\left(\int S_i^T(\boldsymbol{k},\boldsymbol{p},t)\,\mathrm{d}^3\boldsymbol{p}\right), \tag{2.18}$$

with $\int(\ldots)\,\mathrm{d}^3\boldsymbol{p}$ the integration over the whole spectral domain, and where $S_i^T(\boldsymbol{k},\boldsymbol{p},t)$ is the scalar three-point third-order spectral correlation,

$$S_i^T(\boldsymbol{k},\boldsymbol{p},t)\delta(\boldsymbol{k}+\boldsymbol{p}+\boldsymbol{q}) = \mathrm{i}\langle\hat{u}_i(\boldsymbol{q})\hat{\theta}(\boldsymbol{k})\hat{\theta}(\boldsymbol{p})\rangle. \tag{2.19}$$

The scalar flux $F_i(\boldsymbol{k},t)$, or mixed velocity–scalar correlation, introduced in (2.17) is defined as

$$\langle\hat{u}_i^*(\boldsymbol{p})\hat{\theta}(\boldsymbol{k})\rangle = F_i(\boldsymbol{k})\delta(\boldsymbol{k}-\boldsymbol{p}), \tag{2.20}$$

which corresponds to the second-order correlation $R_i^F = \langle u_i\theta\rangle$ in physical space. The scalar flux Craya equation is then

$$\left(\frac{\partial}{\partial t} - A_{jl}k_j\frac{\partial}{\partial k_l} + (\nu+a)k^2\right)F_i(\boldsymbol{k}) + M_{ij}(\boldsymbol{k})F_j(\boldsymbol{k}) + \lambda_j\hat{R}_{ij}(\boldsymbol{k}) = T_i^{F,NL}(\boldsymbol{k}), \tag{2.21}$$

where $T_F^{T,NL}$ is the nonlinear scalar flux transfer, which can be written

$$T_i^{F,NL}(\boldsymbol{k},t) = P_{inm}(\boldsymbol{k})\int S_{nm}^F(\boldsymbol{k},\boldsymbol{p},t)\,\mathrm{d}^3\boldsymbol{p} + k_j\int S_{ji}^{F*}(\boldsymbol{p},\boldsymbol{k},t)\,\mathrm{d}^3\boldsymbol{p}, \tag{2.22}$$

with $S_{nm}^F(\boldsymbol{k},\boldsymbol{p},t)$ the scalar flux three-point third-order spectral correlation,

$$S_{nm}^F(\boldsymbol{k},\boldsymbol{p},t)\delta(\boldsymbol{k}+\boldsymbol{p}+\boldsymbol{q}) = \mathrm{i}\langle\hat{u}_n(\boldsymbol{q})\hat{\theta}(\boldsymbol{k})\hat{u}_m(\boldsymbol{p})\rangle. \tag{2.23}$$

The form of the nonlinear scalar flux transfer (2.22) has been obtained in a recent active scalar study (Burlot *et al.* 2015). Writing $T_i^{F,NL}$ in a manner analogous to the kinetic case (Mons *et al.* 2016) is done by introducing

$$\tau_i^F(\boldsymbol{k},\boldsymbol{p},t) = k_n\int S_{ni}^F(\boldsymbol{k},\boldsymbol{p},t)\,\mathrm{d}^3\boldsymbol{p}, \tag{2.24}$$

so that the nonlinear scalar transfer reads

$$T_i^{F,NL}(\boldsymbol{k},t) = \tau_i^F(\boldsymbol{k},\boldsymbol{p},t) + \tau_i^{*F}(\boldsymbol{p},\boldsymbol{k},t) + W_i^F(\boldsymbol{k},t), \tag{2.25}$$

where $W_i^F(\boldsymbol{k},t) = -\alpha_i\alpha_m\tau_m^F(\boldsymbol{k},\boldsymbol{p},t)$ represents nonlinear mixed pressure–velocity correlations, from which the RTI of F_i is expected, but not prescribed. This RTI mechanism is responsible for the destruction of the scalar flux since it does not exist in isotropic turbulence. The quantity $\tau_i^F + \tau_i^{*F}$ is a conservative transfer quantity with zero integral over $\boldsymbol{k}$.

2.3. *Generalized scalar Lin equations and EDQNM closure*

The generalized Lin equations for the scalar correlation $\mathscr{E}^T$ and the scalar flux F_i can be written

$$\left(\frac{\partial}{\partial t} + 2ak^2\right)\mathscr{E}^T(\boldsymbol{k},t) = T^{T,NL}(\boldsymbol{k},t) + T^{T,L}(\boldsymbol{k},t), \tag{2.26}$$

$$\left(\frac{\partial}{\partial t} + (\nu+a)k^2\right)F_i(\boldsymbol{k},t) = T_i^{F,NL}(\boldsymbol{k},t) + T_i^{F,L}(\boldsymbol{k},t). \tag{2.27}$$

Here $T^{T,L}$ and $T_i^{F,L}$ are the linear passive scalar and scalar flux transfers,

$$T^{T,L}(\boldsymbol{k},t) = A_{jl}k_j\frac{\partial \mathscr{E}^T(\boldsymbol{k},t)}{\partial k_l} - 2\lambda_l F_l(\boldsymbol{k},t), \tag{2.28}$$

$$T_i^{F,L}(\boldsymbol{k},t) = A_{jl}k_j\frac{\partial F_i(\boldsymbol{k},t)}{\partial k_l} - M_{ij}(\boldsymbol{k})F_j(\boldsymbol{k},t) - \lambda_j\hat{R}_{ij}(\boldsymbol{k},t). \tag{2.29}$$

Now, the nonlinear passive scalar and scalar flux transfers $T^{T,NL}$ and $T^{F,NL}$ need to be modelled. The EDQNM approximation was first introduced by Orszag (1970), Leith (1971) and Orszag (1977) for hydrodynamic turbulence.

Hereafter, an EDQNM closure adapted to homogeneous anisotropic flows is derived similarly to Mons *et al.* (2016). The complete anisotropic form of the second-order spectral tensors is kept in the quasi-normal (QN) formulation, and is therefore expressed in terms of the $\boldsymbol{k}$-vector descriptors of table 1, whereas the eddy damping (ED), which models the contribution from fourth-order cumulants to the equations that govern triple correlations, is kept in an isotropic relationship. Assuming that the scalar probability distributions are close to normal distributions, the QN approximation is used to model the passive scalar and scalar flux nonlinear transfers. Then, combining isotropic ED, complete QN and Markovianization allows one to write from (2.18) and (2.22)

$$T^{T,NL}(\boldsymbol{k},t) = 2k_i\int \theta^T_{kpq}\mathfrak{T}_i^{T,QN}(\boldsymbol{k},t)\,\mathrm{d}^3\boldsymbol{p}, \tag{2.30}$$

$$T_i^{F,NL}(\boldsymbol{k},\boldsymbol{p},t) = P_{imn}(\boldsymbol{k})\int \theta^F_{kpq}\mathfrak{T}^F_{nm}(\boldsymbol{k},\boldsymbol{p},t)\,\mathrm{d}^3\boldsymbol{p} + k_j\int \theta^F_{kpq}\mathfrak{T}^{*F}_{ji}(\boldsymbol{p},\boldsymbol{k},t)\,\mathrm{d}^3\boldsymbol{p}. \tag{2.31}$$

Here θ^T_{kpq} and θ^F_{kpq} are the characteristic times of the third-order scalar and scalar flux correlations, respectively,

$$\theta^T_{kpq} = \frac{1-\exp[-(a(k^2+p^2)+\nu q^2+\mu_2(k)+\mu_2(p)+\mu_3(q))t]}{a(k^2+p^2)+\nu q^2+\mu_2(k)+\mu_2(p)+\mu_3(q)}, \tag{2.32}$$

$$\theta^F_{kpq} = \frac{1-\exp[-(ak^2+\nu(p^2+q^2)+\mu_2(k)+\mu_3(p)+\mu_3(q))t]}{ak^2+\nu(p^2+q^2)+\mu_2(k)+\mu_3(p)+\mu_3(q)}, \tag{2.33}$$

and θ^T_{kpq} and θ^F_{kpq} are obtained by writing the evolution equations of the passive scalar and scalar flux third-order correlations defined in (2.19) and (2.23), respectively. Such an approach for the scalar case has already been used by Bos *et al.* (2005) for HITSG. The eddy-damping terms μ_2 and μ_3 reflect departure from normal laws and, combined with Markovianization, ensure realizability,

$$\mu_2(k,t) = A_2\sqrt{\int_0^k p^2E(p,t)\,\mathrm{d}p}, \quad \mu_3(k,t) = A_3\sqrt{\int_0^k p^2E(p,t)\,\mathrm{d}p}, \tag{2.34a,b}$$

with $A_2 = 0$ and $A_3 = 1.3$. The setting of A_2 and A_3 is discussed in Herring *et al.* (1982) and Lesieur (2008), along with the choice of the eddy-damping terms μ_2 and μ_3. These two constants are set, based on experimental and theoretical considerations, to recover the Corrsin–Obukhov constant $K_{CO} \simeq 0.8$. For the kinetic field, the eddy damping used in EDQNM is

$$\mu_1(k,t) = A_1\sqrt{\int_0^k p^2E(p,t)\,\mathrm{d}p}, \tag{2.35}$$

as defined by Pouquet *et al.* (1975) – as an improved version, more general (assessed in two and three dimensions, at various Reynolds numbers) than in Orszag (1970) – where $A_1 = 0.355$, so that the Kolmogorov constant is recovered, $K_0 \simeq 1.3$. As a result of the QN approximation, $\mathfrak{T}_i^{T,QN}$ and $\mathfrak{T}_{ij}^{F,QN}$ can be written

$$\begin{aligned}\mathfrak{T}_i^{T,QN}(\boldsymbol{k},\boldsymbol{p},t) &= 2P_{imn}(\boldsymbol{q})F_n(\boldsymbol{k},t)F_m(\boldsymbol{p},t) + F_i^*(\boldsymbol{q},t)(k_nF_n(\boldsymbol{p},t) + p_nF_n(\boldsymbol{k},t)) \\ &\quad - k_n\hat{R}_{ni}(\boldsymbol{q},t)(\mathscr{E}^T(\boldsymbol{k},t) - \mathscr{E}^T(\boldsymbol{p},t)), \qquad (2.36)\\ \mathfrak{T}_{ij}^{F,QN}(\boldsymbol{k},\boldsymbol{p},t) &= k_n(\hat{R}_{ni}(\boldsymbol{q},t)F_j^*(\boldsymbol{p},t) + \hat{R}_{nj}(\boldsymbol{p},t)F_i^*(\boldsymbol{q},t)) \\ &\quad + 2F_m(\boldsymbol{k},t)(P_{imn}(\boldsymbol{q})\hat{R}_{nj}(\boldsymbol{p},t) + P_{jmn}(\boldsymbol{p})\hat{R}_{ni}(\boldsymbol{q},t)). \qquad (2.37)\end{aligned}$$

With this closure, and with calculations very similar to the kinetic case, the nonlinear scalar transfer becomes

$$\begin{aligned}T^{T,NL}(\boldsymbol{k},t) &= 2\int \theta_{kpq}^T kp(xy+z)(\mathscr{E}'' + \mathrm{Re}\,X'')(\mathscr{E}'^T - \mathscr{E}^T)\,\mathrm{d}^3\boldsymbol{p} \\ &\quad + 2\int \theta_{kpq}^T \left(k_nF_n'^*(p_mF_m + k_mF_m') + p_mF_mk_nF_n'\frac{ky-px}{q}\right)\mathrm{d}^3\boldsymbol{p}. \qquad (2.38)\end{aligned}$$

The single and double primes $'$ and $''$ refer to wavevectors $\boldsymbol{p}$ and $\boldsymbol{q}$, respectively; x, y and z are cosines of the angles formed by the triad vectors $(\boldsymbol{k},\boldsymbol{p},\boldsymbol{q})$; and $X = Ze^{2i\lambda}$, $X' = Z'e^{2i\lambda'}$ and $X'' = Z''e^{2i\lambda''}$, where λ, λ' and λ'' are rotation angles of the triad around $\boldsymbol{k}$, $\boldsymbol{p}$ and $\boldsymbol{q}$, respectively, and Z has been defined in (2.6). Since the scalar flux exists only in an anisotropic configuration, and is thus a purely anisotropic field, the second part of (2.38) is neglected for moderately anisotropic flows, where all quadratic anisotropic contributions can be neglected. The closure for $F_i(\boldsymbol{k})$ is developed with an appropriate decomposition in the following section.

3. Spherically averaged scalar Lin equations

This section presents the final step of the modelling. Spherically averaged evolution equations for the scalar variance spectrum, the scalar directivity and the scalar flux are derived from the previous generalized scalar Lin equations (2.26) and (2.27). These final scalar equations depend only on the modulus k of the wavevector $\boldsymbol{k}$.

3.1. *Spherically averaged descriptors*

A decomposition similar to the one of $\mathscr{E}$ in the kinetic case is used for the scalar correlation

$$\mathscr{E}^T(\boldsymbol{k},t) = \frac{E_T(k,t)}{4\pi k^2}(1 - 15H_{ij}^{(T)}(k,t)\alpha_i\alpha_j) = \mathscr{E}_0^T(\boldsymbol{k},t) + \mathscr{E}^{(T,dir)}(\boldsymbol{k},t), \qquad (3.1)$$

with $\mathscr{E}^{(T,dir)} = -15\mathscr{E}_0^T H_{ij}^{(T)}\alpha_i\alpha_j$ and $\mathscr{E}_0^T = E_T/(4\pi k^2)$. The following decomposition is chosen for the scalar flux:

$$F_i(\boldsymbol{k},t) = \tfrac{3}{2}\mathscr{E}_j^F(k,t)P_{ij}(\boldsymbol{k}). \qquad (3.2)$$

This decomposition is consistent with the scalar flux being a solenoidal field ($k_iF_i = 0$). These equations (3.1) and (3.2) are exact in HITSG (Herr *et al.* 1996), whereas they are truncations at the first non-trivial order (the second order) of the scalar correlation

$\mathscr{E}^T$ and scalar flux F_i expansions for the cases involving mean velocity gradients (HST and HSTSG). These truncations are consistent with the modelling of $\mathscr{E}$ and Z done in (2.8) and (2.9), respectively.

Hermitian symmetry for the scalar flux, $F_i(-\boldsymbol{k}) = F_i^*(\boldsymbol{k})$, is straightforward from the decomposition of a vector into helical modes. Notably, it implies that the vector $\mathscr{E}_j^F$ is purely real. About the distinction between directional and polarization anisotropies: scalars admit directional anisotropy only. Consequently, $H_{ij}^{(T)}$, which appears in the expansion of $\mathscr{E}^T$, reflects directional anisotropy, as does $H_{ij}^{(dir)}$ in the decomposition of $\mathscr{E}$. Then, as F_i is a vector, $\mathscr{E}_j^F$ represents polarization anisotropy. Finally, a solenoidal second-order tensor such as $\hat{R}_{ij}$ admits both contributions (Cambon & Rubinstein 2006). This classification is summarized in table 1.

An additional solenoidal contribution in terms of the Levi-Civita permutation tensor is discussed by O'Gorman & Pullin (2005), resulting in the so-called quadrature spectrum. It can be shown that, using a toroidal–poloidal decomposition of a solenoidal vector, the latter contribution is redundant with the projection part in (3.2). Therefore, as the helicity spectrum (Gomez, Politano & Pouquet 2000) is neglected in the spectral Reynolds stress tensor, this additional solenoidal contribution is consistently discarded.

The scalar anisotropic descriptor $H_{ij}^{(T)}$ and the spherically averaged scalar flux E_i^F are defined similarly to the kinetic ones $H_{ij}^{(dir)}$ and $H_{ij}^{(pol)}$ using spherical integration,

$$2E_T(k,t)H_{ij}^{(T)}(k,t) = \int_{S_k} \mathscr{E}^{(T,dir)}(\boldsymbol{k},t)P_{ij}\,\mathrm{d}^2\boldsymbol{k}, \tag{3.3}$$

$$E_i^F(k,t) = \int_{S_k} F_i(\boldsymbol{k},t)\,\mathrm{d}^2\boldsymbol{k}. \tag{3.4}$$

The scalar anisotropy tensor b_{ij}^T is then given by

$$b_{ij}^T(t) = \frac{1}{K_T(t)}\int_0^\infty E_T(k,t)H_{ij}^{(T)}(k,t)\,\mathrm{d}k, \tag{3.5}$$

and is analogous in the description of anisotropy to $b_{ij}^{(dir)}$ for the velocity field (Mons *et al.* 2016). Similar scalar anisotropy descriptors were introduced by Kassinos *et al.* (2007), with a slightly different convention for structure-based modelling. Finally, the scalar energy K_T, or scalar variance, and its dissipation rate are defined as

$$K_T(t) = \langle\theta^2\rangle = \int_0^\infty E_T(k,t)\,\mathrm{d}k, \quad \epsilon_T(t) = 2a\int_0^\infty k^2E_T(k,t)\,\mathrm{d}k. \tag{3.6a,b}$$

3.2. *Spherical average of the passive scalar and scalar flux fields*

The final evolution equations for the spherically averaged scalar descriptors, derived from the previous generalized Lin equations, and briefly called spherically averaged scalar Lin equations, read

$$\left(\frac{\partial}{\partial t} + 2ak^2\right)E_T(k,t) = S^{T,NL(iso)}(k,t) + S^{T,L(iso)}(k,t), \tag{3.7}$$

$$\left(\frac{\partial}{\partial t} + 2ak^2\right)E_T(k,t)H_{ij}^{(T)}(k,t) = S_{ij}^{T,NL(dir)}(k,t) + S_{ij}^{T,L(dir)}(k,t), \tag{3.8}$$

$$\left(\frac{\partial}{\partial t} + (a+\nu)k^2\right)E_i^F(k,t) = S_i^{F,NL}(k,t) + S_i^{F,L}(k,t). \tag{3.9}$$

Here $S^{T,NL(iso)}$ is the classical nonlinear spherically averaged isotropic scalar transfer,

$$\begin{aligned} S^{T,NL(iso)}(k,t) &= \int_{S_k} T^{T,NL}(\boldsymbol{k},t)\,\mathrm{d}^2\boldsymbol{k} \\ &= \int_{\Delta_k} 16\theta^T_{kpq}\pi^2k^2p^2q(xy+z)\mathscr{E}_0''(\mathscr{E}_0'^T-\mathscr{E}_0^T)\,\mathrm{d}p\,\mathrm{d}q, \end{aligned} \tag{3.10}$$

which is exactly the one derived by Lesieur (2008); and $S^{T,NL(dir)}_{ij}$ is the nonlinear spherically averaged directional scalar transfer,

$$\begin{aligned} S^{T,NL(dir)}_{ij}(k,t) &= \frac{1}{2}\int_{S_k} T^{T,NL}P_{ij}(\boldsymbol{k},t)\,\mathrm{d}^2\boldsymbol{k} - \frac{\delta_{ij}}{3}S^{T,NL(iso)}(k,t) \\ &= \int_{\Delta_k} 4\pi^2\theta^T_{kpq}k^2p^2q(xy+z)(y^2-1)\mathscr{E}_0''(\mathscr{E}_0'^T-\mathscr{E}_0^T)H_{ij}''^{(pol)}\,\mathrm{d}p\,\mathrm{d}q \\ &\quad + \int_{\Delta_k} 8\pi^2\theta^T_{kpq}k^2p^2q(xy+z)(3y^2-1)\mathscr{E}_0''(\mathscr{E}_0'^T-\mathscr{E}_0^T)H_{ij}''^{(dir)}\,\mathrm{d}p\,\mathrm{d}q \\ &\quad + \int_{\Delta_k} 8\pi^2\theta^T_{kpq}k^2p^2q(xy+z)\mathscr{E}_0''((3z^2-1)\mathscr{E}_0'^TH_{ij}'^{(T)}-2\mathscr{E}_0^TH_{ij}^{(T)})\,\mathrm{d}p\,\mathrm{d}q, \end{aligned} \tag{3.11}$$

with Δ_k the domain where k, p and q are the moduli of the triad vectors. The transfer $S^{T,NL(iso)}$ is a conservative transfer, meaning that its integral over k is zero. However, the integral of $S^{T,NL(dir)}_{ij}$ is different from zero (like the directional transfer of the velocity field). From the non-conservative part of $S^{T,NL(dir)}_{ij}$, an RTI of the passive scalar is expected. Nevertheless, as there is no fluctuating pressure in the passive scalar equation, it cannot return to isotropy on its own, and therefore this mechanism is driven by the dynamics of the velocity field only. For the linear terms, $S^{T,L(iso)}$ is the linear spherically averaged isotropic scalar transfer,

$$S^{T,L(iso)}(k,t) = \int_{S_k} T^{T,L}(\boldsymbol{k},t)\,\mathrm{d}^2\boldsymbol{k} = -2A^+_{ln}\frac{\partial}{\partial k}(kE_TH^{(T)}_{ln}) - 2\lambda_lE^F_l, \tag{3.12}$$

and $S^{T,L(dir)}_{ij}$ is the linear spherically averaged directional scalar transfer,

$$\begin{aligned} S^{T,L(dir)}_{ij}(k,t) &= \frac{1}{2}\int_{S_k} T^{T,L}(\boldsymbol{k},t)P_{ij}\,\mathrm{d}^2\boldsymbol{k} - \frac{\delta_{ij}}{3}S^{T,L(iso)}(k,t) \\ &= -\frac{3}{7}E_T\left(A^+_{ij}H^{(T)}_{il}+A^+_{li}H^{(T)}_{jl}-\frac{2}{3}A^+_{ln}\delta_{ij}H^{(T)}_{ln}\right)+\frac{1}{5}A^+_{ij}E_T \\ &\quad +\frac{2}{7}\left(A^+_{il}\frac{\partial}{\partial k}(kE_TH^{(T)}_{jl})+A^+_{jl}\frac{\partial}{\partial k}(kE_TH^{(T)}_{il})-\frac{2}{3}A^+_{lm}\delta_{ij}\frac{\partial}{\partial k}(kE_TH^{(T)}_{lm})\right) \\ &\quad -\frac{1}{15}A^+_{ij}\frac{\partial}{\partial k}(kE_T)-E_T(A^-_{lj}H^{(T)}_{il}+A^-_{li}H^{(T)}_{jl}) \\ &\quad -\frac{1}{10}\left(\lambda_iE^F_j+\lambda_jE^F_i-\frac{2}{3}\lambda_lE^F_l\delta_{ij}\right), \end{aligned} \tag{3.13}$$

where A^+_{ij} and A^-_{ij} respectively denote the symmetric and antisymmetric parts of the velocity mean-gradient matrix, λ_i is the mean scalar gradient and $E^F_i = 4\pi k^2\mathscr{E}^F_i$.

Regarding the scalar flux, its nonlinear transfer becomes, at first order in anisotropy,

$$
\begin{aligned}
T_i^{F,NL}(\boldsymbol{k},t) = \frac{3}{2}\int \theta^F_{kpq} k \mathscr{E}_0' \,[\, & \mathscr{E}_j^F \,(\, 2px(\alpha_i + z\alpha_i')(\alpha_j'' + y\alpha_j) \\
& + q(y+xz)(2\alpha_i''(\alpha_j'' + y\alpha_j) - P_{ij})\,) + k\mathscr{E}_j^{F''}((1-z^2)P_{ij}'' + (\alpha_i + z\alpha_i')(\alpha_j + y\alpha_j''))\,]\ \mathrm{d}^3\boldsymbol{p} \\
& + \frac{3}{2}\int \theta^F_{pkq} k\,[\, q\mathscr{E}_0\mathscr{E}_j^{F'}(\alpha_i'' + y\alpha_i)(\alpha_j + z\alpha_j' + 2y(\alpha_j'' + x\alpha_j')) \\
& + k\mathscr{E}_0''\mathscr{E}_j^{F'}((\alpha_i + y\alpha_i'')(\alpha_j + z\alpha_j') + (1-y^2)(P_{ij}' - 2\alpha_i(\alpha_j + z\alpha_j'))) \\
& + p(\mathscr{E}_0\mathscr{E}_j^{F''}(\alpha_i' + z\alpha_i)(\alpha_j + y\alpha_j'') - (xy+z)\mathscr{E}_0''\mathscr{E}_j^F P_{ij})\,]\ \mathrm{d}^3\boldsymbol{p} \\
& - 3\int \theta^F_{kpq} k\alpha_i\,[\, k(1-y^2)\mathscr{E}_0''\mathscr{E}_j^{F'}(\alpha_j + z\alpha_j') \\
& + q\mathscr{E}_0'\mathscr{E}_j^F(1 - z^2 - 2y(y+xz))(\alpha_j'' + y\alpha_j)\,]\ \mathrm{d}^3\boldsymbol{p}. \qquad (3.14)
\end{aligned}
$$

One can observe that in the framework of moderate anisotropy, only the isotropic part of the velocity field $\mathscr{E}_0 = E/(4\pi k^2)$ remains. The nonlinear spherically averaged scalar flux transfer is then

$$
\begin{aligned}
S_i^{F,NL}(k,t) &= \int_{S_k} T_i^{F,NL}(\boldsymbol{k},t)\,\mathrm{d}^2\boldsymbol{k} \\
&= 4\pi^2 \int_{\Delta_k} \theta^F_{kpq} k^2 pq \mathscr{E}_0'[k\mathscr{E}_i^{F''}(1 + y^2 - z^2 - xyz - 2y^2z^2) - 2q(y^3 + xz)\mathscr{E}_i^F]\,\mathrm{d}p\,\mathrm{d}q \\
&\quad + 4\pi^2 \int_{\Delta_k} \theta^F_{pkq} k^2 pq\,[\, \mathscr{E}_0(qz(2xy^2 + yz - x)\mathscr{E}_i^{F'} - py(x+yz)\mathscr{E}_i^{F''}) \\
&\quad + k\mathscr{E}_0''((1 - y^2 + z^2 - xyz - 2y^2z^2)\mathscr{E}_i^{F'} - 2(1-y^2)\mathscr{E}_i^F)\,]\ \mathrm{d}p\,\mathrm{d}q. \qquad (3.15)
\end{aligned}
$$

One can extract from this nonlinear scalar-flux transfer the mixed pressure–velocity part, which is expected to have an RTI function

$$
S_i^{F,RTI}(k,t) = -8\int_{\Delta_k} \pi^2 \theta^F_{kpq} k^3 pq \mathscr{E}_0' \mathscr{E}_i^{F''}(1-y^2)(1-z^2)\,\mathrm{d}p\,\mathrm{d}q. \qquad (3.16)
$$

And $S_i^{F,L}$ is the spherically averaged linear scalar flux transfer,

$$
\begin{aligned}
S_i^{F,L}(k,t) &= \int_{S_k} T_i^{F,L}(\boldsymbol{k},t)\,\mathrm{d}^2\boldsymbol{k} \\
&= -2\lambda_j E\left(\frac{1}{3}\delta_{ij} + H_{ij}^{(dir)} + H_{ij}^{(pol)}\right) - \frac{1}{5}A_{ij}^{+}\left(2E_j^F + \frac{\partial}{\partial k}(kE_j^F)\right). \qquad (3.17)
\end{aligned}
$$

As a conclusion, the dynamics of a passive scalar field in homogeneous anisotropic turbulence is driven by six spherically averaged compact equations within this anisotropic EDQNM modelling: three for the velocity field first given in Mons *et al.* (2016),

$$
\left(\frac{\partial}{\partial t} + 2\nu k^2\right) E(k,t) = S^{NL(iso)}(k,t) + S^{L(iso)}(k,t), \qquad (3.18)
$$

$$\left(\frac{\partial}{\partial t}+2\nu k^2\right)E(k,t)H_{ij}^{(dir)}(k,t)=S_{ij}^{NL(dir)}(k,t)+S_{ij}^{L(dir)}(k,t), \tag{3.19}$$

$$\left(\frac{\partial}{\partial t}+2\nu k^2\right)E(k,t)H_{ij}^{(pol)}(k,t)=S_{ij}^{NL(pol)}(k,t)+S_{ij}^{L(pol)}(k,t), \tag{3.20}$$

two for the passive scalar (equations (3.7) and (3.8)), and one for the scalar flux (equation (3.9)). The last three are original results of the present work. The different anisotropy descriptors are gathered in table 1.

3.3. *Numerical parameters, initial conditions and validity of the model*

The time evolution of the kinetic spectra (E, $EH_{ij}^{(dir)}$, $EH_{ij}^{(pol)}$) and the passive scalar and scalar flux spectra (E_T, $E_TH_{ij}^{(T)}$, E_i^F) are obtained by solving 20 coupled integro-differential equations using a third-order Runge–Kutta scheme with implicit treatment of diffusion terms. The wavenumber space is discretized using a logarithmic mesh $k_{i+1}=10^{1/f}k_i$ for $1\leqslant i\leqslant n$, where n is the number of modes and $f=17$ is the number of discrete points per decade. This mesh spans from k_{min} to $k_{max}=10k_\eta$, where $k_\eta=(\epsilon/\nu^3)^{1/4}$ is the Kolmogorov wavenumber. Such a resolution at high Reynolds numbers allows a fine description of the viscous range, with k_{min} higher than the ones usually used in DNS. The time step is monitored by defining a constant Courant–Friedrichs–Lewy (CFL) number and is obtained by considering the characteristic time scales of scalar and kinetic dynamics. The values of the physical and numerical parameters are given for simulations at large and small Reynolds numbers in table 2. If not mentioned otherwise, the initial conditions are isotropic ($F_i(k,t=0)=0$) with the kinetic energy spectrum $E(k,\,t=0)$ proposed by Pope (2000) and Meyers & Meneveau (2008),

$$E(k,t=0)=K_0k^{-5/3}\epsilon^{2/3}f_L(kL)f_\eta(k\eta), \tag{3.21}$$

where f_L and f_η are shape functions for large and small scales, respectively,

$$f_L(x)=\left(\frac{x}{(x^{1.5}+1.5-\sigma/4)^{2/3}}\right)^{5/3+\sigma},\quad f_\eta(x)=\exp(-5.3((x^4+0.4^4)^{1/4}-0.4)), \tag{3.22a,b}$$

and σ is the infrared slope. Simulations have shown that initial moderately anisotropic conditions only slightly impact the early dynamics, without altering the asymptotic states. Thus, classical isotropic initial conditions are used such as $E_T(k,0)=E(k,0)$, avoiding the introduction of supplementary numerical parameters.

In what follows, the Prandtl number is equal to one, meaning that $a=\nu$, and integrated quantities correspond to quantities obtained by integration over the whole wavenumber space, such as the kinetic energy.

It has been mentioned several times that the present model is valid for moderate anisotropy as quadratic contributions in terms of anisotropy descriptors have been neglected. In this view, criteria need to be given to quantify the upper bounds of the anisotropy that the model can handle at the levels of the velocity and scalar fields. Such criteria, or realizability conditions, can be derived directly from (2.8) and (3.1), to ensure that the kinetic and scalar energy densities $\mathscr{E}$ and $\mathscr{E}^T$ are positive. This yields

$$\max_{i=1,2,3}(\mathscr{L}_i)\leqslant\tfrac{1}{15},\quad \max_{i=1,2,3}(\mathscr{L}_i^T)\leqslant\tfrac{1}{15}, \tag{3.23a,b}$$

Kind of anisotropy	$Re_\lambda(t=0)$	Pr	CFL	k_{min}	k_{max}
HITSG	10^4	1	0.3	$10^{-7}k_L(t=0)$	$10k_\eta$
HITSG towards low Re	10^4	1	0.3	$10^{-16}k_L(t=0)$	$10k_\eta$
HST	1	1	0.3	$10^{-10}k_L(t=0)$	10^5k_η
HSTSG	1	1	0.3	$10^{-10}k_L(t=0)$	10^5k_η

TABLE 2. Physical and numerical parameters used for the simulations. Here k_L and k_η are the integral and Kolmogorov wavenumbers, respectively. The initial value of the Reynolds number $Re_\lambda = K\sqrt{20/3\nu\epsilon}$ can be different when it comes to comparisons with experiments and DNS, along with the Prandtl number, often set to 0.7.

where $\mathscr{L}_i$ and $\mathscr{L}_i^T$ are eigenvalues of $H_{ij}^{(dir)}$ and $H_{ij}^{(T)}$, respectively. In the following simulations, these realizability conditions are *a posteriori* systematically verified as satisfied. Moreover, it is worth noting that the violation of (3.23) immediately yields negative values for the spectra $E(k, t)$ and $E_T(k, t)$. Hence, moderate anisotropy could be roughly defined as the case for which the intensity of the mean-field gradients is such that the realizability conditions are satisfied.

4. Comparisons with experiments and DNS

In the two previous sections, spherically averaged evolution equations were derived to investigate the dynamics of a passive scalar and its flux in homogeneous anisotropic turbulence. The modelling of anisotropy within the complete EDQNM approach, labelled as EDQNM in what follows, is now assessed by comparisons to several DNS and experiments at moderate Reynolds numbers in the three configurations presented in the introduction: HITSG, HST and HSTSG. In each case, definitions and basic results are recalled. In what follows, the infrared range refers to very large scales, and, from this point, large-scale kinetic and scalar infrared slopes are the same, i.e. $\sigma = \sigma_T$. This is justified in appendix A, and these infrared slopes are defined as $E(k < k_L, t) \sim k^\sigma$ and $E_T(k < k_T, t) \sim k^{\sigma_T}$, with k_L and k_T the integral kinetic and scalar wavenumbers, respectively.

4.1. *Homogeneous isotropic turbulence with a mean scalar gradient (HITSG)*

In this section, the emphasis is put on the specific case where the scalar flux appears due to a uniform mean gradient $\lambda_j = (0, 0, -\Lambda)$ with $\Lambda > 0$, whereas the velocity field is purely isotropic and decreases with time. This configuration has been widely investigated (Bos *et al.* 2005; O'Gorman & Pullin 2005; Bos 2014): turbulent eddies bring the hot fluid to the cold parts of the flow (and the opposite), thus creating a turbulent flux.

4.1.1. *Definitions and spectral behaviour*

Firstly, some definitions are given. When the kinetic field is isotropic, it tends to destroy the scalar flux F_i, whose dynamics is given by (3.4) and (3.9), created by the scalar gradient Λ. Given the form of the production transfer term $S_i^{F,L}$, only the third component of E_i^F is non-zero, and its sign is opposite to that of Λ. Hence, the cospectrum is defined by

$$\mathscr{F}(k, t) = E_3^F(k, t). \tag{4.1}$$

The cospectrum energy and cospectrum dissipation rate are straightforwardly

$$K_{\mathscr{F}}(t) = \int_0^\infty \mathscr{F}(k,t)\,\mathrm{d}k, \quad \epsilon_{\mathscr{F}}(t) = (\nu + a)\int_0^\infty k^2 \mathscr{F}(k,t)\,\mathrm{d}k. \tag{4.2a,b}$$

Finally, in homogeneous turbulence, the time evolution of the velocity–scalar correlation $R_i^F(t) = \langle u_i\theta\rangle$ is

$$\frac{\mathrm{d}R_i^F}{\mathrm{d}t} + R_{ij}\Lambda_j + A_{ij}R_j^F = \left\langle p\frac{\partial\theta}{\partial x_i}\right\rangle - \epsilon_i^F, \tag{4.3}$$

with $A_{ij} = 0$ in HITSG, and

$$\epsilon_i^F(t) = (\nu + a)\left\langle \frac{\partial u_i}{\partial x_l}\frac{\partial\theta}{\partial x_l}\right\rangle, \quad \epsilon_{\mathscr{F}} = \epsilon_3^F. \tag{4.4a,b}$$

In the case of a simple scalar gradient ($R_3^F = K_{\mathscr{F}}$), the previous evolution equation simplifies into

$$\frac{\mathrm{d}K_{\mathscr{F}}}{\mathrm{d}t}(t) = P_{\mathscr{F}}(t) - \epsilon_{\mathscr{F}}(t) + \Pi_{\mathscr{F}}(t), \tag{4.5}$$

where

$$\Pi_{\mathscr{F}}(t) = \int_0^\infty S_3^{F,NL}(k,t)\,\mathrm{d}k \tag{4.6}$$

is the cospectrum destruction, or cospectrum pseudo-RTI, driven by the fluctuating pressure of the kinetic field. Here $P_{\mathscr{F}}$ is the cospectrum production

$$P_{\mathscr{F}}(t) = \int_0^\infty S_3^{F,L}(k,t)\,\mathrm{d}k = \frac{2}{3}\Lambda K(t). \tag{4.7}$$

In homogeneous isotropic turbulence with a scalar gradient (HITSG), the cospectrum is initially zero. The spectral scaling of the cospectrum can be deduced by dimensional analysis, as proposed by Lumley (1967), Bos *et al.* (2005) and O'Gorman & Pullin (2005). One has to assume that $\mathscr{F}$ depends only on the scalar gradient Λ, the wavenumber k and the kinetic energy dissipation rate ϵ so that

$$\mathscr{F}(k,t) = C_{\mathscr{F}}\Lambda\epsilon^{1/3}k^{-7/3}, \tag{4.8}$$

where $C_{\mathscr{F}}$ is the cospectrum constant, found to be $C_{\mathscr{F}} \simeq 3$ in the present work. Bos *et al.* (2005) reported $C_{\mathscr{F}} \simeq 1.5$ whereas O'Gorman & Pullin (2005) computed $C_{\mathscr{F}} = 3.5$ with their asymptotic high-Reynolds-number model. The $k^{-7/3}$ scaling is similar to the velocity cross-component spectral tensor in shear turbulence (Lumley 1967). If one assumes that $\mathscr{F}$ depends on ϵ, k and its dissipation rate $\epsilon_{\mathscr{F}}$, then $\mathscr{F} \sim \epsilon^{-1/3}\epsilon_{\mathscr{F}}k^{-5/3}$, which is similar to a passive scalar variance spectrum scaling. This approach would imply that the cospectrum dissipation rate $\epsilon_{\mathscr{F}}$ is conserved throughout the cascade and this cannot be satisfied due to the pressure effects (Bos *et al.* 2004).

In what follows, for numerical simulations, one needs to define a dimensionless mean scalar gradient $\mathscr{S}_\theta$. There are different possibilities to define a reference mean scalar gradient Λ_{ref}, unlike the mean velocity gradient, which is unambiguously

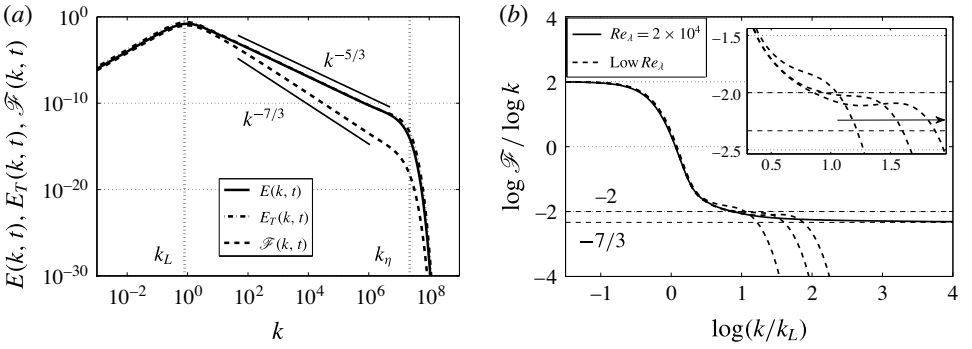

FIGURE 1. (*a*) Cospectrum, kinetic energy and scalar spectra $\mathscr{F}$, E and E_T for $Re_\lambda = 2 \times 10^5$, as a function of the wavenumber k, along with the integral and Kolmogorov wavenumbers k_L and k_η. (*b*) Effects of low Reynolds numbers on the scaling of $\mathscr{F}$, obtained with $\log \mathscr{F} / \log k$, as a function of $\log(k/k_L)$, with a zoom on the narrow inertial range for the low-Re_λ curves $Re_\lambda = 50$, 100 and 150: the arrow indicates the sense of increasing Reynolds numbers. Both for Saffman turbulence ($\sigma = 2$).

defined (De Souza, Nguyen & Tavoularis 1995). The dimensionless mean scalar gradient is defined as

$$\mathscr{S}_\theta = \frac{\Lambda}{\Lambda_{ref}}. \tag{4.9}$$

The reference mean scalar gradient Λ_{ref} is defined explicitly in the following comparisons. If not mentioned otherwise, $\mathscr{S}_\theta = 1$ is chosen.

In figure 1, the $k^{-7/3}$ scaling clearly appears for the cospectrum. However, as previously reported by Bos *et al.* (2005), it requires a high Reynolds number ($Re_\lambda \geqslant 10^4$ here). This condition is very important. Indeed, without it, there is no clear power law, neither $k^{-7/3}$ nor k^{-2}, as revealed in figure 1 for the three moderate-Reynolds-number cases $50 \leqslant Re_\lambda \leqslant 150$. The inertial range is rather narrow, and there is a transitory slope that tends to $-7/3$ as Re_λ increases. Hence, the k^{-2} scaling reported in previous works seems to be a low-Reynolds-number effect, which occurs around $Re_\lambda = 100$, typical for DNS. The $k^{-7/3}$ scaling has also been obtained experimentally (Mydlarski 2003), in DNS (O'Gorman & Pullin 2005; Watanabe & Gotoh 2007) or with classical EDQNM (Bos *et al.* 2005; Bos & Bertoglio 2007).

An interesting point to mention, which has not been explicitly reported so far, is about the infrared range of the cospectrum. Indeed, as $\mathscr{F} = 0$ in the initial isotropic flow, one can wonder how it evolves at very large scales. The result is displayed in figure 2: the cospectrum infrared exponent is the same as the kinetic one σ. This is important for the results presented in § 5. Moreover, the $k^{-7/3}$ scaling is recovered for all the σ presented. Finally, the linear and nonlinear transfers associated with the cospectrum are presented in figure 2: $S_3^{F,NL} - S_3^{F,RTI}$ represents the conservative nonlinear transfer with zero integral over k, where $S_3^{F,RTI}$ is the RTI transfer associated with pressure effects, and $S_3^{F,NL}$ is the total nonlinear transfer that corresponds to a non-conservative flux because of the RTI mechanism. And $S_3^{F,L}$ is the linear transfer responsible for production of anisotropy through the scalar gradient, which decreases with time as the kinetic spectrum $E(k,t)$.

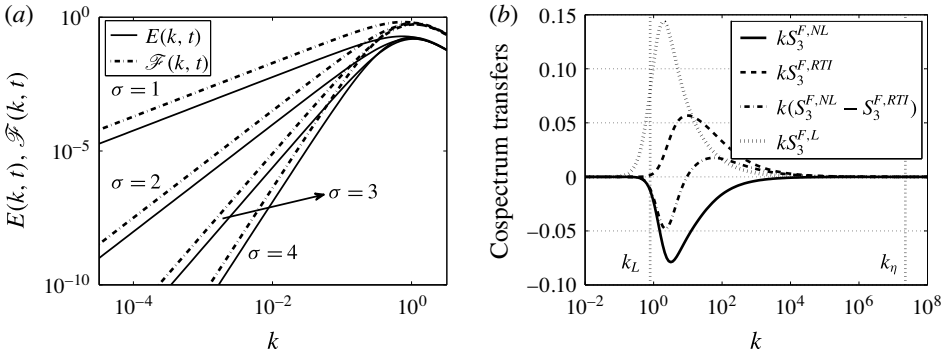

FIGURE 2. (*a*) Large-scale spectral scaling of the cospectrum $\mathscr{F}$ for different kinetic infrared slopes σ after several turnover times, as a function of the wavenumber k. (*b*) Linear and nonlinear transfers of the cospectrum for $\sigma = 2$ at $Re_\lambda = 2 \times 10^5$ as a function of the wavenumber k.

4.1.2. *Comparison with Overholt & Pope (1996)*

The focus is put on the ratio of the cospectrum dissipation $\epsilon_{\mathscr{F}}$ and cospectrum production $P_{\mathscr{F}}$. In the DNS of Overholt & Pope (1996), it is shown that the cospectrum dissipation is not negligible at low Reynolds number even though it decreases with Re_λ. The following power law is found:

$$\left(\frac{\epsilon_{\mathscr{F}}}{P_{\mathscr{F}}}\right)^{DNS} = 4.61 Re_\lambda^{-0.769} \tag{4.10}$$

for four different DNS from $Re_\lambda = 28$ to 185. This is reported in figure 3 along with results from the present anisotropic EDQNM simulations for comparison purposes:

$$\left(\frac{\epsilon_{\mathscr{F}}}{P_{\mathscr{F}}}\right)^{EDQNM} = 11.6 Re_\lambda^{-0.760}. \tag{4.11}$$

In the present case, this ratio is evaluated for Reynolds numbers such that the kinetic field decreases according to CBC theory (Comte-Bellot & Corrsin 1966). The satisfactory agreement with DNS regarding the Re_λ power law for low Reynolds numbers partially validates the model for the cospectrum. The discrepancy for the numerical factor may arise from the fact that in the DNS the velocity field is forced, whereas it is freely decaying here. The interesting result is that the Re_λ power law is valid in both decaying and forced turbulence, and does not depend on the infrared slope σ. As for the high-Reynolds-number regime, the Re_λ^{-1} predicted by Bos *et al.* (2005) is recovered numerically in figure 3 as well. This scaling law can be obtained analytically by direct computation, assuming that for high Reynolds numbers the dominant region of the kinetic spectrum and cospectrum is the inertial range,

$$\frac{\epsilon_{\mathscr{F}}(t)}{P_{\mathscr{F}}(t)} = \frac{3(\nu + a)}{2\Lambda} \frac{\displaystyle\int_0^\infty k^2 \mathscr{F}(k,t)\,\mathrm{d}k}{\displaystyle\int_0^\infty E(k,t)\,\mathrm{d}k} \sim \frac{\epsilon^{1/3} \displaystyle\int_{k_L}^{k_\eta} k^{-1/3}\,\mathrm{d}k}{\epsilon^{2/3} \displaystyle\int_{k_L}^{k_\eta} k^{-5/3}\,\mathrm{d}k}. \tag{4.12}$$

Then, using classical relations such as $(k_\eta/k_L) = Re_L^{3/4}$, where Re_L is the integral Reynolds number, so that $\sqrt{20 Re_L/3} = Re_\lambda$, and $\nu k_\eta^{4/3} = \epsilon^{1/3}$, one finds $\epsilon_{\mathscr{F}}/P_{\mathscr{F}} \sim Re_\lambda^{-1}$.

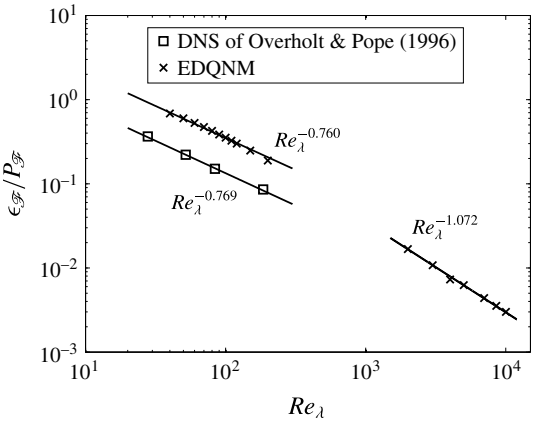

FIGURE 3. Comparison with the DNS by Overholt & Pope (1996) of the ratio of cospectrum dissipation $\epsilon_{\mathscr{F}}$ and production $P_{\mathscr{F}}$, both defined in (4.4) and (4.7), for high and low Reynolds numbers, as a function of the Reynolds number Re_λ. Simulations for $\sigma = 2$ and $\mathscr{S}_\theta = 1$. Symbols $\times$ and $\square$ represent respectively EDQNM simulations and DNS. Lines are best-fit power laws.

4.1.3. *Comparison with Sirivat & Warhaft (1983)*

In this section, results provided by the present model are compared with the experimental work of Sirivat & Warhaft (1983) in the HITSG configuration in figure 4. The case where the scalar gradient is created with a mandoline (a screen of thin heated wires) is considered. The parameters of the experiment are the following ones: the input velocity is $U = 3.4$ m s^{-1} and the mesh size $M = 0.024$ m. For this configuration, the initial Reynolds number is $Re_\lambda(0) = 26.4$ and the turnover time $\tau_{exp} = 1.14$ s. The scalar dissipation rate is evaluated to approximately $\epsilon_\theta \simeq 10^{-2}\,^\circ\mathrm{C}^2$ s^{-1} for a scalar gradient $\beta = 1.78\,^\circ$C m^{-1}. Assuming that for this experiment the Prandtl number is approximately 0.7, a reference fluctuating scalar gradient is computed as

$$\Lambda_{ref} = \left(\frac{\partial\theta}{\partial x}\right)_{ref} = \sqrt{\frac{\epsilon_\theta}{3a}}, \tag{4.13}$$

so that the dimensionless mean scalar gradient is $\mathscr{S}_\theta = \beta/\Lambda_{ref} = 0.152$. Temporal results are transposed to spatial ones through

$$\frac{x}{M} = \frac{t}{\tau_0}\frac{U\tau_{exp}}{M}, \tag{4.14}$$

where τ_0 is the kinetic characteristic time K/ϵ evaluated numerically after two turnover times, so that transition effects from the initial conditions are erased. The experimental decay rate of the kinetic field being $\alpha_{exp} = -1.3$, Saffman turbulence ($\sigma = 2$) is an appropriate large-scale initial condition for the EDQNM simulations. The cospectrum correlation

$$\rho_{u_i\theta} = \frac{\langle u_i\theta\rangle}{\sqrt{\langle u_i^2\rangle\langle\theta^2\rangle}}, \quad \rho_{w\theta} = \rho_{u_3\theta}, \tag{4.15a,b}$$

is well recovered and $\rho_{w\theta} \to -0.7$. The ratio of scalar production $-\Lambda K_{\mathscr{F}}$ and dissipation ϵ_T is also in agreement with present results. The final value of the ratio

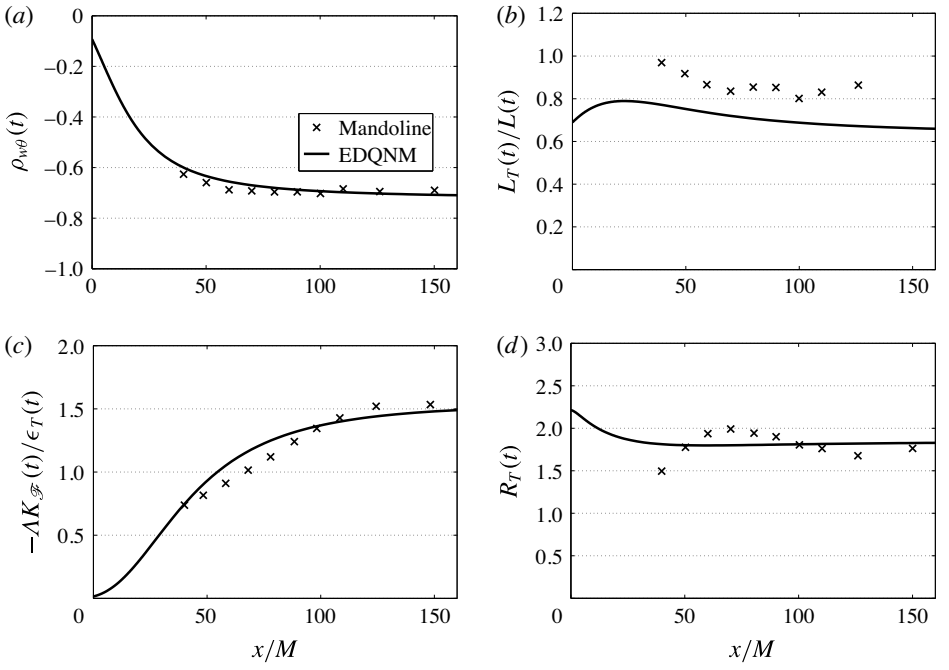

FIGURE 4. Comparisons with experimental results of Sirivat & Warhaft (1983) for the case of the mandoline, as a function of x/M, where M is the mesh size and x the distance to the grid. The $\times$ symbols correspond to the experimental results and lines to the EDQNM ones. (*a*) The cospectrum correlation $\rho_{w\theta}$ defined in (4.15). (*b*) The scalar to kinetic integral scales ratio L_T/L. (*c*) Ratio of production and dissipation of the passive scalar $-\Lambda K_{\mathscr{F}}/\epsilon_T$. (*d*) Kinetic to scalar time scales ratio R_T defined in (4.16).

of characteristic times,

$$R_T = \frac{K\epsilon_T}{K_T\epsilon}, \tag{4.16}$$

matches quite well with experimental data. However, there is a slight difference for the ratio of integral scales L_T/L ($\simeq 0.7$ with the present anisotropic EDQNM closure, and $\simeq 0.9$ experimentally). As no indications are given, there could simply be a difference in the definitions; nevertheless, the fact that $L_T(t) < L(t)$ is recovered. Let us underline that the initial condition is isotropic here, which is not the case in the experiment: as mentioned by Sirivat & Warhaft (1983), the initial fluctuating temperature field is slightly inhomogeneous, and because of the grid itself the kinetic field contains some anisotropy. But still, the early times of $\rho_{w\theta}$ and $-\Lambda K_{\mathscr{F}}/\epsilon_T$ are well captured. As for the cospectrum correlation $\rho_{w\theta}$, it has to be pointed out that there is a large scatter, since measured values span from approximately -0.19 to approximately -0.8, with an average around approximately -0.65 (Venkataramani & Chevray 1978; Sirivat & Warhaft 1983; Overholt & Pope 1996; Mydlarski 2003). It appears in EDQNM simulations that $\rho_{w\theta}$ varies strongly for $5 \leqslant Re_\lambda \leqslant 300$, roughly from 0.6 for high Re to approximately 0.71 for low Re. This is the classical range of Reynolds numbers covered by experiments and DNS. Consequently, the reason for the scattering of $\rho_{w\theta}$ could be moderate Reynolds numbers, where it becomes more sensitive to the intensity of the mean-scalar gradient.

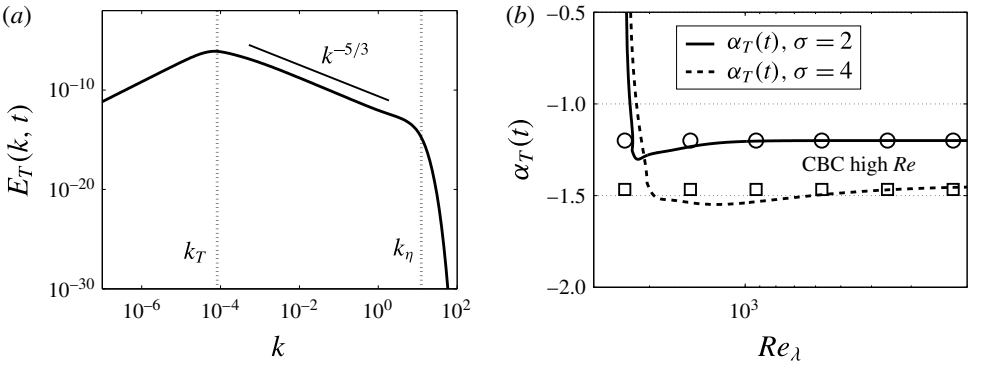

FIGURE 5. (*a*) Scalar spectrum $E_T(k,t)$ in a sustained shear flow, with $St = 50$ ($Re_\lambda = 10^4$) and $\sigma = 2$, along with the scalar integral and Kolmogorov wavenumbers k_T and k_η, as a function of the wavenumber k. (*b*) Scalar decay exponents α_T in high-Reynolds-number regime, with $St = 1$ for $\sigma = 2$ and $\sigma = 4$, as a function of the Reynolds number Re_λ. Symbols represent the theoretical values expected from (4.17): ○ is for $\sigma = \sigma_T = 2$, and □ is for $\sigma = \sigma_T = 4$.

4.2. *Homogeneous shear turbulence (HST)*

In this section, qualitative comparisons and general results are given for the passive scalar field submitted to a shear without any scalar gradient. This particular framework has not received much attention in experiments or DNS, unlike the case with both velocity and scalar gradients that will be addressed in the next section. Firstly, the case of a mean shear imposed at short times only and then released is investigated, and finally the emphasis is put on the passive scalar field submitted to a sustained shear. For a shear-driven flow, the mean velocity gradient matrix is written $A_{13} = \mathrm{d}U_1/\mathrm{d}x_3 = -S$ with $S > 0$. The dimensionless time St refers to the quantity of anisotropy injected in the flow. In both cases, the scalar spectrum displays a $k^{-5/3}$ inertial–convective range as revealed in figure 5.

4.2.1. *Case of the shear-released turbulence*

In isotropic turbulence, the decay exponents of scalar integrated quantities such as the scalar variance K_T and the scalar dissipation rate ϵ_T are well known since Comte-Bellot & Corrsin (1966) and are recalled in table 3 following the work of Briard *et al.* (2015). For the scalar variance,

$$K_T(t) \sim t^{\alpha_T}, \quad \alpha_T = -2\frac{\sigma_T - p_T + 1}{\sigma - p + 3}, \tag{4.17}$$

where $p_T(\sigma = \sigma_T = 4) = 0.27$ and $p_T(\sigma = \sigma_T \leqslant 3) = 0$, and $p(\sigma = 4) = 0.55$ and $p(\sigma \leqslant 3) = 0$. These parameters p and p_T reflect the strong backscatter of energy for the velocity and scalar fields, respectively, that can occur in the infrared range notably for the Batchelor case. In particular, p_T depends slightly on the Prandtl number and much more on the kinetic infrared slope σ (Briard *et al.* 2015). In figure 5, large-Reynolds-number scalar decay exponents are recovered for Saffman and Batchelor shear-released turbulence. This means that initial large-scale velocity gradients do not alter the long-time decay of scalar integrated quantities. Such a result for the scalar field is similar to what was found for the velocity one (Briard *et al.* 2016).

	High-Re regime	Low-Re regime
$K(t)$	$\alpha = -2\dfrac{\sigma - p + 1}{\sigma - p + 3}$	$\alpha = -\dfrac{\sigma + 1}{2}$
$\epsilon(t)$	$n_\epsilon = -3\dfrac{\sigma - p + 5/3}{\sigma - p + 3}$	$n_\epsilon = -\dfrac{\sigma + 3}{2}$
$L(t)$ and $L_T(t)$	$n_L = \dfrac{2}{\sigma - p + 3}$	$n_L = \dfrac{1}{2}$
$K_T(t)$	$\alpha_T = -2\dfrac{\sigma_T - p_T + 1}{\sigma - p + 3}$	$\alpha_T = -\dfrac{\sigma_T + 1}{2}$
$\epsilon_T(t)$	$n_{\epsilon_T} = -\dfrac{\sigma - p + 5 + 2\sigma_T - 2p_T}{\sigma - p + 3}$	$n_{\epsilon_T} = -\dfrac{\sigma_T + 3}{2}$
Re_λ	$n_{Re_\lambda} = -\dfrac{1}{2}\dfrac{\sigma - p - 1}{\sigma - p + 3}$	$n_{Re_\lambda} = -\dfrac{\sigma - 1}{8}$

TABLE 3. Kinetic and scalar decay exponents in homogeneous isotropic turbulence. Here σ and σ_T are the kinetic and scalar infrared slopes; p and p_T are the kinetic and scalar backscatter parameters; and $Re_\lambda = K\sqrt{20/3\nu\epsilon}$ is the Reynolds number based on the Taylor micro-scale. The kinetic and scalar integrated quantities are: kinetic energy $K = \int E\,\mathrm{d}k$; kinetic energy dissipation rate $\epsilon = 2\nu\int k^2 E\,\mathrm{d}k$; kinetic integral scale $4L = 3\pi K^{-1}\int k^{-1}E\,\mathrm{d}k$; scalar variance $K_T = \int E_T\,\mathrm{d}k$; scalar variance dissipation rate $\epsilon_T = 2a\int k^2 E_T\,\mathrm{d}k$; and scalar integral scale $2L_T = \pi K_T^{-1}\int k^{-1}E_T\,\mathrm{d}k$.

Before the release of the velocity gradients $S = 1\tau_0^{-1}$ at $t = 1\tau_0$, the scalar anisotropy indicators b_{ij}^T depart from the isotropic value 0. Then the passive scalar field experiences an RTI mechanism driven by the velocity field. This process is displayed in figure 6. An asymptotic anisotropic state is reached, similar to the kinetic one (Speziale *et al.* 1990; Mons *et al.* 2016). The final non-zero values of b_{ij}^T show that there is still anisotropy in the flow after the release of the velocity gradients A_{ij}. The spectral anisotropy tensors $H_{ij}^{(T)}(k, t)$ are also displayed in figure 6, and reveal that anisotropy is mostly gathered around the scalar integral wavenumber k_T. The interesting point is that some anisotropy persists in the small scales of the scalar second-order moments, as shown in the zoom. Simulations indicate that small scales of the velocity second-order moments are completely isotropic. This is in agreement with most of DNS and experiments.

A supplementary qualitative comparison, in the case of mean-velocity-gradient released flow for the passive scalar field, can be made. Indeed, an axisymmetric contraction is performed by Gylfason & Warhaft (2009), where the temperature fluctuations are created by a mean gradient. Although no quantitative comparison is possible because of the moderate anisotropy limitation of the present model (the dimensionless velocity gradient reaches $\mathscr{S} = 70$ in Gylfason & Warhaft (2009)), interesting qualitative facts can be reported. The measure of anisotropy is done using the fluctuating scalar covariance $C_{ij} = \langle \xi_i \xi_j \rangle$, where $\xi_i = \partial\theta/\partial x_i$, which brings the same kind of information as do the b_{ij}^T. During the contraction, $|C_{ij}|$ increases, and at the exit of the contraction, it converges to a constant value, different from zero. This behaviour is similar to that of the b_{ij}^T, and Gylfason & Warhaft (2009) concluded that there is a partial RTI, which is in agreement with the present results.

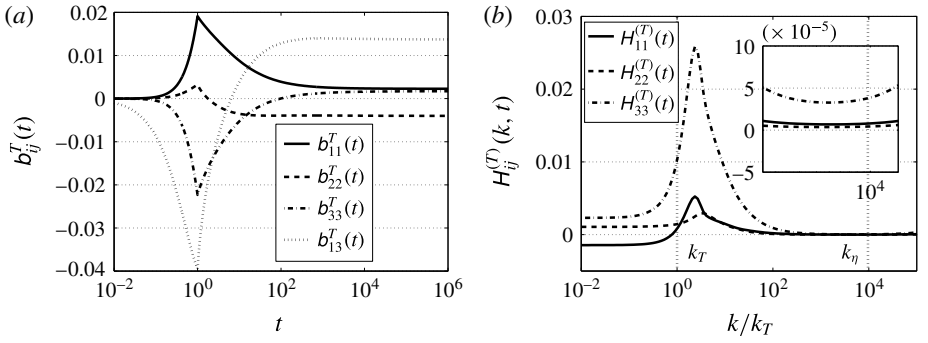

FIGURE 6. Scalar anisotropy indicators for $\sigma = 2$, with $St = 1$: (*a*) $b_{ij}^T(t)$, defined in (3.5), as a function of time t; (*b*) $H_{ij}^{(T)}(k, t)$, defined in (3.3), at $t = 10^6\tau_0$ ($Re_\lambda = 800$), along with the scalar integral and Kolmogorov wavenumbers k_T and k_η, as a function of the normalized wavenumber k/k_T.

4.2.2. *Case of the sustained-shear turbulence*

In this section, the shear is maintained. It is known that there is an exponential growth of the kinetic energy $K(t)$ due to nonlinear transfers (De Souza *et al.* 1995; Garg & Warhaft 1998; Brethouwer 2005; Sagaut & Cambon 2008; Mons *et al.* 2016). The kinetic exponential growth rate is

$$\gamma = 2b_{13} - \frac{\epsilon}{KS}, \tag{4.18}$$

which directly comes from the evolution equation of $K(t)$, where $b_{13} = R_{13}/(2K)$. The estimation due to the present modelling (Mons *et al.* 2016) gives $\gamma \simeq 0.34$. This seemingly high value of γ is discussed in Briard *et al.* (2016). The relevant question is now: Is there a similar growth for the scalar variance $K_T(t)$? Its evolution is governed by the equation

$$\frac{\mathrm{d}K_T}{\mathrm{d}t} = 2\Lambda K_{\mathscr{F}}(t) - \epsilon_T(t). \tag{4.19}$$

In HST, $\Lambda = 0$ and there is no production term linked to velocity gradients, unlike the evolution equation of $K(t)$. Hence, there should be no growth of $K_T(t)$ even if the shear is maintained. In figure 7, the b_{ij}^T and the scalar shear rapidity

$$S_R^T(t) = \frac{\epsilon_T(t)}{SK_T(t)} \tag{4.20}$$

reach constant values for $St \geqslant 30$. Moreover, it can be seen in figure 7 that the scalar variance K_T decreases exponentially, with a decay rate $\gamma_T \simeq -0.52$. Let us replace K_T and ϵ_T in (4.19) by

$$K_T(t) = K_T^\infty \exp(\gamma_T St), \quad \epsilon_T(t) = \epsilon_T^\infty \exp(\gamma_T St). \tag{4.21a,b}$$

An analytical expression for γ_T is then obtained:

$$\gamma_T = -\frac{\epsilon_T^\infty}{SK_T^\infty}, \quad K_T(t) \sim K_T(0) \exp(\gamma_T St). \tag{4.22a,b}$$

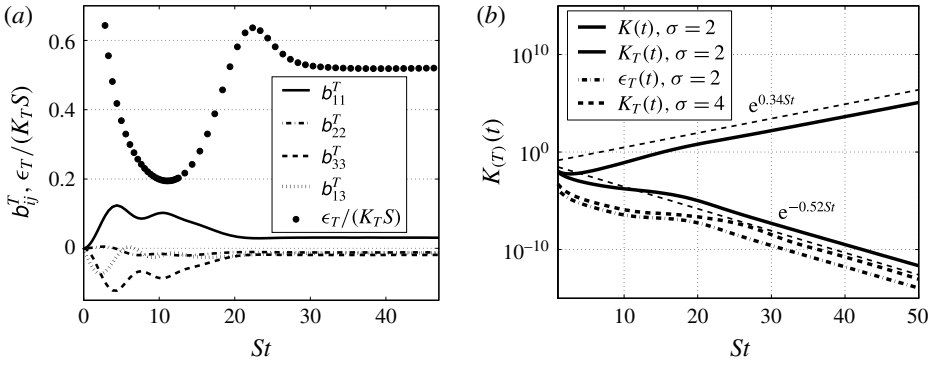

FIGURE 7. Evolution of integrated quantities in HST, as a function of the accumulated anisotropy St, with $S = 1\tau_0^{-1}$ and $Re_\lambda(St = 50) \sim 10^4$. (*a*) Scalar anisotropy indicators b_{ij}^T, defined in (3.5), along with $S_R^T = \epsilon_T/(K_T S)$ for $\sigma = 2$. (*b*) Kinetic and scalar energies K and K_T, and scalar dissipation rate ϵ_T, for $\sigma = 2$ and $\sigma = 4$.

The decay rate γ_T found by plotting K_T is in good agreement with the asymptotic value of S_R^T, which also gives $\gamma_T = -0.52$. The important result here is that the value of the scalar exponential decay rate γ_T seems not to depend on the shear rate S for moderate intensity, nor on the infrared exponents σ and σ_T (and neither does γ for the exponential growth of $K(t)$ (Briard *et al.* 2016)). The scalar dissipation ϵ_T, also displayed in figure 7, exponentially decreases with the same rate $\gamma_T = -0.52$, which is consistent with the evolution equation (4.19).

The fact that anisotropy created by mean velocity gradients accelerates the decay of the scalar field has been observed experimentally by Warhaft (1980) with a contraction. Moreover, such an exponential decrease of the scalar variance K_T has been found theoretically by Gonzalez (2000) using a self-preservation analysis. The exponential decay rate obtained is $\beta'_\theta = -(S\tau_\theta)^{-1}$ with $\tau_\theta = K_T/\epsilon_\theta$, which is precisely the γ_T obtained here.

Various simulations show that the realizability condition (3.23) is violated at the scalar level for $S > 3\tau_0^{-1}$, whereas it still holds at the velocity level. This shows that pure shear flows might be a limiting case of the present anisotropic EDQNM modelling for the passive scalar dynamics. Hopefully, this case is less studied and less representative of atmospheric flows than the HSTSG one, which is the topic of the next section: when a mean scalar gradient is added to the mean shear, the large-scale anisotropy at the scalar level is smoothed and the scalar field can handle higher shear rates.

4.3. *Homogeneous shear turbulence with a mean scalar gradient (HSTSG)*

This final section focuses on homogeneous shear turbulence with a mean scalar gradient (HSTSG). The emphasis is put on the impact of both mean velocity and scalar gradients on the scalar flux and the passive scalar.

4.3.1. *Definitions and transfers*

Previously, it was shown that, with a mean scalar gradient λ_3, only the third component of the scalar flux $E_3^F = \mathscr{F}$ was non-zero. With a velocity gradient only,

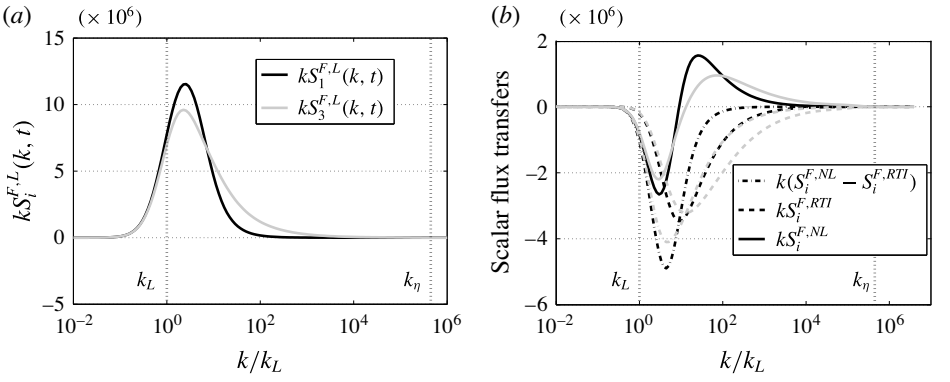

FIGURE 8. Linear (a) and nonlinear (b) transfers for the cospectrum ($i = 3$, grey) and streamwise flux ($i = 1$, black) for $\sigma = 2$ at $St = 50$, where $Re_\lambda = 2 \times 10^4$, and as a function of the normalized wavenumber k/k_L.

no scalar flux appears at all. With both velocity and scalar gradients, the first component of the scalar flux is also non-zero. Therefore, the streamwise flux is defined as

$$E_1^F(k,t) = \mathscr{F}_S(k,t), \tag{4.23}$$

which arises only with the additional presence of a velocity gradient $\mathrm{d}U_1/\mathrm{d}x_3$. Its energy and dissipation rate are then

$$K_{\mathscr{F}}^S(t) = \int_0^\infty \mathscr{F}_S(k,t)\,\mathrm{d}k, \quad \epsilon_{\mathscr{F}}^S(t) = (\nu + a)\int_0^\infty k^2 \mathscr{F}_S(k,t)\,\mathrm{d}k. \tag{4.24a,b}$$

In figure 8, both linear and nonlinear spherically averaged transfers are presented for the cospectrum and the streamwise flux. One can note that they are very similar and only slightly vary in intensity. This shows that the two components of the scalar flux behave similarly in HSTSG. The small-scale RTI of scalar second-order moments in the HSTSG framework is discussed later, and the spectral scaling of $\mathscr{F}_S$ is addressed after the comparisons.

4.3.2. *Comparison with Rogers et al. (1989)*

Now, the comparison is made with the DNS of Rogers *et al.* (1989). There, the velocity gradient $\mathrm{d}U_1/\mathrm{d}x_2$ is such that the dimensionless shear rate is $\mathscr{S} = 14.142$, so that $\mathrm{d}U_1/\mathrm{d}x_2 = S = \mathscr{S}\tau_0^{-1}$ (see De Souza *et al.* (1995) for the process). Three cases for the scalar gradient are performed, one in each direction x_1, x_2 and x_3, with the dimensionless mean scalar gradient $\mathscr{S}_\theta = 2.5$. Comparisons are made with the diffusivity tensor

$$D_{ij}(t) = -\langle \theta u_i \rangle \left(\frac{\mathrm{d}T}{\mathrm{d}x_j}\right)^{-1}. \tag{4.25}$$

Each column of the tensor D_{ij} refers to a different simulation where the direction of the scalar gradient changes. For instance, D_{13} refers to the third case. The agreement between EDQNM simulations and DNS is revealed in figure 9, where D_{ij} is normalized by D_{22}. A difference is observed along the flow direction for D_{11}/D_{22} where DNS predicts a higher value. This discrepancy may come from the

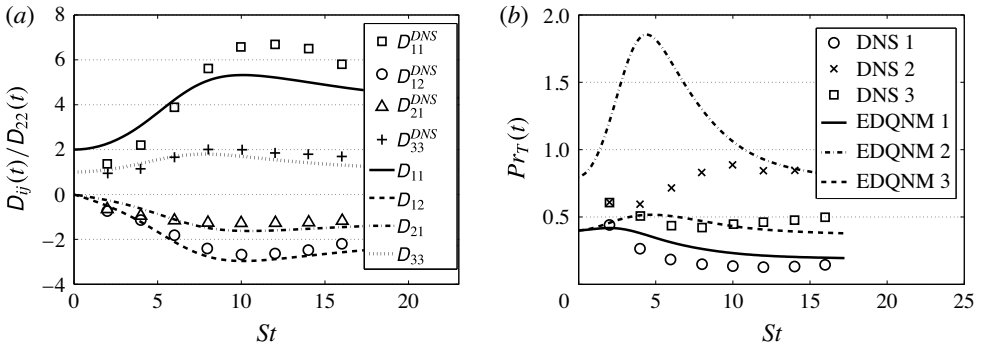

FIGURE 9. Comparisons with numerical results of Rogers *et al.* (1989), with $\sigma = 2$, $\mathscr{S} = 14.142$ and $\mathscr{S}_\theta = 2.5$, as a function of the accumulated anisotropy St. Symbols correspond to the DNS, and lines to the EDQNM simulations. (*a*) The normalized diffusivity tensor, defined in (4.25), for the three orientations of the mean scalar gradient. (*b*) The turbulent Prandtl number Pr_T, defined in (4.26), for these three cases.

limited DNS resolution, which alters the dynamics in the streamwise direction. Then, for each simulation, the turbulent Prandtl number is defined as

$$Pr_T(t) = -\frac{R_{12}}{SD_{ii}}, \quad \text{with no summation on } i, \tag{4.26}$$

where D_{ii} is the turbulent diffusivity, with $i = 1$, 2 or 3 depending on the case considered. The agreement is rather good: the asymptotic value of $Pr_T \simeq 0.8$ is recovered in the second case, whereas the general behaviour is captured for the first and third cases: $Pr_T^{(1)} < Pr_T^{(3)} < Pr_T^{(2)}$.

4.3.3. *Comparison with Kassinos et al. (2007)*

A last comparison is performed with the more recent DNS of Kassinos *et al.* (2007). This work deals with magnetohydrodynamics (MHD) but the validation is made in the purely hydrodynamic case with the data of Brethouwer (2005). Hence, only the case where the magnetic field is zero and where there is no rotation is considered. The mean velocity and scalar gradients are along x_2 and such that $\mathscr{S} = 8.95$ and $\mathscr{S}_\theta = 1$. The kinetic field is allowed to decay without any forcing before velocity and scalar gradients are applied at t_0. There, the Reynolds number is $Re_\lambda = 45$ with $SK/\epsilon(t = t_0) = 18$. The scalar fluctuations are set to 0 at $t = t_0$ (this is why initially $\rho_{v\theta}(t = t_0) = -1$). For EDQNM simulations, the mean gradients are applied after two turnover times and there $SK/\epsilon = 13$ and $Re_\lambda = 50$. The two correlations $\rho_{u\theta}$ and $\rho_{v\theta}$ are presented in figure 10 along with

$$\beta = \frac{S}{\Lambda}\sqrt{\frac{3K_T}{2K}}, \tag{4.27}$$

which characterizes the relative strengths of the velocity and scalar fluctuations. There is a good agreement for the asymptotic values of $\rho_{u\theta}$ and $\rho_{v\theta}$, and the transitory behaviours are rather well captured. The weaker value for $\rho_{u\theta}$ at moderate St may be the consequence of a slightly too strong increase for our $R_{11} = \langle u_1 u_1 \rangle$. This does not prevent the correct value being reached at larger St in the asymptotic state. As for

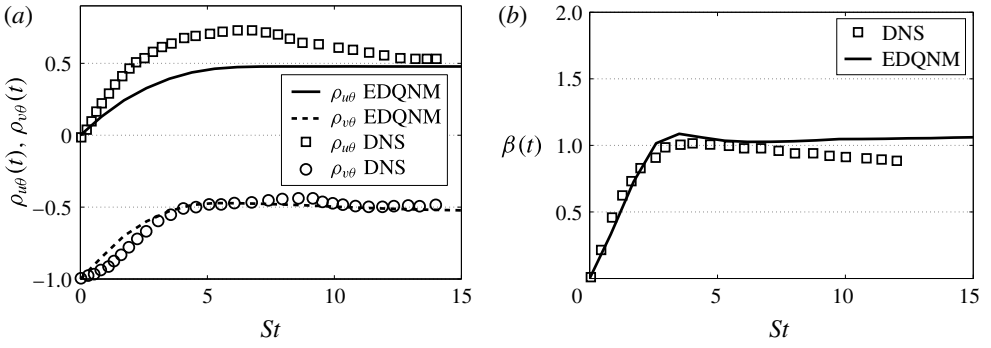

FIGURE 10. Comparisons with the numerical results of Kassinos *et al.* (2007), for $\sigma = 2$, $\mathscr{S} = 8.95$ and $\mathscr{S}_\theta = 1$, as a function of the accumulated anisotropy St. Symbols correspond to DNS and lines to EDQNM simulations. (*a*) Both $\rho_{u\theta}$ and $\rho_{w\theta}$, defined in (4.15), are investigated. (*b*) Here β defined in (4.27) is shown.

β, the simulation differs slightly from the DNS: the β value is over-estimated and has almost reached a constant value whereas it decreases slightly for Kassinos *et al.* (2007). Nevertheless, in both cases $\beta \sim 1$ at large St, which indicates that the velocity and scalar fluctuations have a similar contribution to the anisotropic asymptotic state.

An additional comparison with the pioneering experiment of Tavoularis & Corrsin (1981) is proposed in appendix B: this comparison does not appear in the core of the text since it investigates quantities such as $\rho_{u_i\theta}$, β and Pr_T that have already been studied here. Nevertheless, this experimental work is an important historical contribution, often used as a basis of comparisons, that deserves to be addressed.

4.4. *Conclusion on the comparisons*

The present anisotropic EDQNM modelling for the passive scalar and its flux has been compared with several experiments and DNS. The agreement between asymptotic values of integrated quantities, and even sometimes in the transitory state, validate the modelling introduced in §§ 2 and 3. Nevertheless, it has to be mentioned that the present model seems to slightly under-estimate the turbulent Prandtl number.

5. Decay and growth laws in homogeneous anisotropic turbulence

In this section, the anisotropic EDQNM modelling is used to address the high-Reynolds-number regimes of HAT. This section focuses on the decay and growth of the cospectrum energy and scalar variance in HITSG. From a physical point of view, information about the dominant mechanisms during the decay is given. Moreover, the scaling of the scalar spectra is investigated and the small-scale anisotropy is discussed for both HITSG and HSTSG.

5.1. *Decay and growth laws in HITSG*

The results presented here are an extension of an analysis previously applied to the passive scalar in HIT (Briard *et al.* 2015). The theoretical decay exponents of kinetic and scalar integrated quantities are recalled in table 3.

The cospectrum $\mathscr{F}$ is continuously destroyed by the decay of the velocity field, and is consequently also decaying. Theoretical decay exponents can be derived similarly

to what Comte-Bellot & Corrsin did for the passive scalar. Two assumptions, based on physical arguments for high Reynolds numbers, are needed. Firstly, figure 2 revealed that the cospectrum infrared dynamics is driven only by the kinetic one. Then, we assume that the main contribution to the decay mechanism comes from the inertial range and consequently that only the $k^{-7/3}$ inertial range should be taken into account to determine the decay exponents of $\mathscr{F}$. Secondly, in the case of Batchelor turbulence, when the permanence of the large-eddy hypothesis is broken, backscatter parameters p and p_T are introduced for the velocity and scalar fields, respectively, in HIT (Briard *et al.* 2015). Since $\mathscr{F}$ is the spectral counterpart of the velocity–scalar cross-correlation, its backscatter parameter $p_{\mathscr{F}}$ should contain both effects. Hence, one defines $p_{\mathscr{F}} = (p + p_T)/2$ for $\sigma = 4$ (so that $p_{\mathscr{F}} = 0$ for $\sigma \leqslant 3$). This gives $p_{\mathscr{F}} = 0.4075$ in the case $Pr = 1$ for $\sigma = 4$. These reasonable assumptions yield

$$K_{\mathscr{F}}(t) \sim \int_{k_L}^{\infty} \mathscr{F}(k, t)\, \mathrm{d}k \sim k_L^{-4/3} \epsilon^{1/3}. \tag{5.1}$$

Injecting in this equation the decay exponents of ϵ and k_L recalled in table 3, and using $p_{\mathscr{F}}$, one obtains the theoretical decay exponent of the cospectrum for high Reynolds numbers,

$$K_{\mathscr{F}}(t) \sim t^{\alpha_{\mathscr{F}}}, \quad \alpha_{\mathscr{F}} = -\frac{\sigma - p_{\mathscr{F}} - 1}{\sigma - p + 3}. \tag{5.2}$$

In the low-Reynolds-number regime, when the cospectrum survives, the production term $P_{\mathscr{F}}$ drives the dynamics of the velocity–scalar correlation. The RTI term $\Pi_{\mathscr{F}}$ and the cospectrum dissipation rate $\epsilon_{\mathscr{F}}$ can be considered as negligible. Indeed, considering the form of the cospectrum dissipation (4.4), this quantity reaches its highest values in the inertial range, which tends to disappear for low Reynolds numbers. Therefore, the evolution equation (4.5) of the cospectrum energy becomes $(\mathrm{d}K_{\mathscr{F}}/\mathrm{d}t) \sim P_{\mathscr{F}} = 2\Lambda K/3$. This immediately yields

$$\alpha_{\mathscr{F}} = -\frac{\sigma - 1}{2}, \tag{5.3}$$

which does not depend on the scalar gradient Λ.

These theoretical decay exponents for the cospectrum for high and low Reynolds numbers are assessed numerically in figure 11. The agreement is excellent, even for the particular case of Batchelor turbulence. Such laws could not have been observed before since it requires high Reynolds numbers in decaying turbulence, whereas most of the DNS of HITSG consider a stationary velocity field at moderate Reynolds numbers. These theoretical results, assessed numerically, give further insights into the prediction of high-Reynolds-number decay in HITSG. From (5.2) and (5.3), it follows that $K_{\mathscr{F}}$ does not decay for $\sigma = 1$. In this case, the Reynolds number Re_λ remains constant and so the dynamics of the inertial range, on which $\alpha_{\mathscr{F}}$ is based, remains unchanged.

The dissipation rate $\epsilon_{\mathscr{F}}$ is now investigated. Probably because the scalar flux is a purely anisotropic quantity, which implies that $\epsilon_{\mathscr{F}}$ is not conserved in the inertial range, unlike ϵ and ϵ_T, one cannot express its time dependence as a power law. Nevertheless, as the inertial range disappears for low Reynolds numbers, obtaining

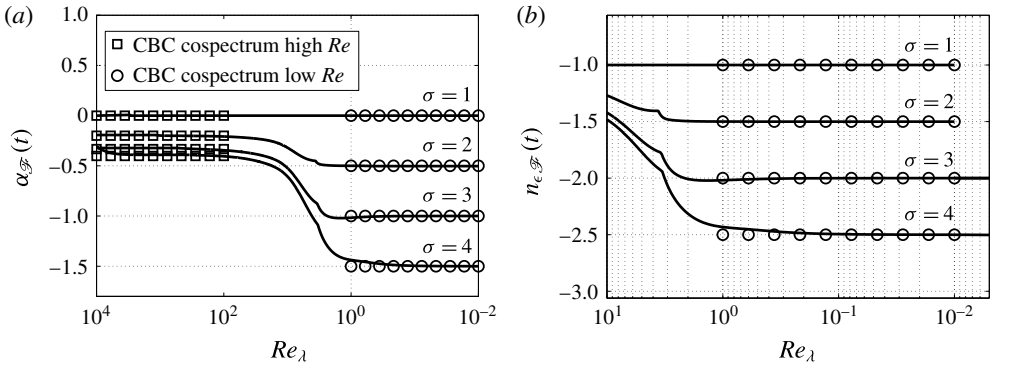

FIGURE 11. Decay exponents of the cospectrum energy $\alpha_{\mathscr{F}}$ (*a*) and of the cospectrum dissipation $n_{\epsilon_{\mathscr{F}}}$ (*b*) for different infrared slopes σ, as a function of the Reynolds number Re_λ. Symbols represent theoretical predictions: □ for high Reynolds numbers, given by (5.2); ○ for low Reynolds numbers, given by (5.3) and (5.4).

the decay exponent $n_{\epsilon_{\mathscr{F}}}$ of $\epsilon_{\mathscr{F}}$ is possible in this regime, considering the evolution equation (4.5), so that

$$\epsilon_{\mathscr{F}}(t) \sim t^{n\epsilon_{\mathscr{F}}}, \quad n_{\epsilon_{\mathscr{F}}} = \alpha_{\mathscr{F}} - 1 = -\frac{\sigma+1}{2}. \tag{5.4}$$

The agreement between this theoretical result and numerical simulations is displayed in figure 11 as well.

The emphasis is now put on the effect of the mean scalar gradient Λ on the passive scalar itself. The scalar spectrum still displays a $k^{-5/3}$ inertial–convective range despite the mean gradient, as revealed in figure 1, and this was obtained experimentally as well (Mydlarski & Warhaft 1998). From the evolution equation of the scalar variance (4.19), it follows that the dynamics of K_T is driven by the production term in the presence of a mean scalar gradient Λ. Using the previous results regarding the decay exponents of $K_{\mathscr{F}}$, the theoretical exponent of K_T in the presence of a mean scalar gradient α_T^Λ can be found. In the high-Reynolds-number regime, one has

$$K_T(t) \sim t^{\alpha_T^\Lambda}, \quad \alpha_T^\Lambda = \frac{4 + p_{\mathscr{F}} - p}{\sigma - p + 3} > 0, \tag{5.5}$$

and for low Reynolds numbers,

$$\alpha_T^\Lambda = -\frac{\sigma - 3}{2}. \tag{5.6}$$

Note that the exponents do not depend explicitly on the scalar gradient Λ. The agreement between these theoretical expressions of α_T^Λ and numerical simulations is presented in figure 12 in both high- and low-Reynolds-number regimes. For high Reynolds numbers, the scalar variance grows in time whatever σ is, whereas for low Reynolds numbers, it decays only for $\sigma = 4$. This can be explained using some physical arguments. The theoretical prediction (5.6) of α_T^Λ is based on the fact that the dynamics of K_T is driven by the production term $2\Lambda K_{\mathscr{F}}$, and $K_{\mathscr{F}}$ is greater for smaller σ. Consequently, for high infrared slope such as $\sigma = 4$, the spectrum $E(k, t)$,

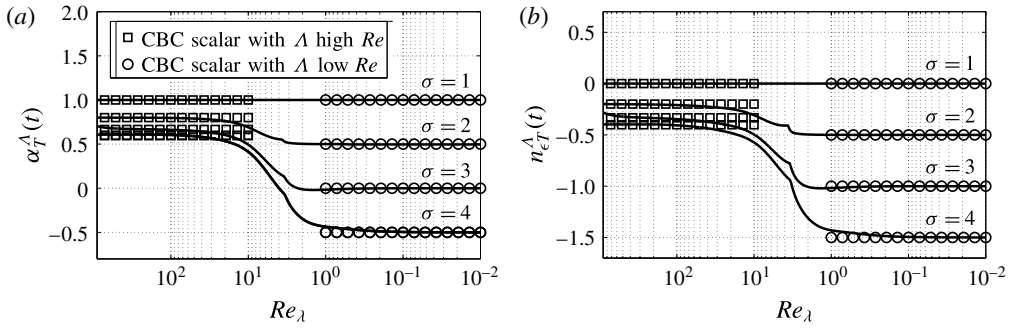

FIGURE 12. Growth and decay exponents of the scalar energy α_T^Λ (*a*) and of the scalar dissipation rate $n_{\epsilon_T}^\Lambda$ (*b*) for different infrared slopes σ, as a function of the Reynolds number Re_λ. Symbols represent theoretical predictions: □ for high Reynolds numbers, given by (5.5); ○ for low Reynolds numbers, given by (5.6).

and thus $\mathscr{F}(k, t)$, has less energy in large scales, resulting in a weak production term for the scalar variance that does not balance dissipation. This is consistent with HITSG experimental results at moderate Re_λ, where the scalar variance can grow or decay depending on the intensity of Λ: with a weak Λ, K_T still decays (nevertheless more slowly than in HIT). Therefore, a strong mean scalar gradient Λ corresponds to a small infrared slope σ, or equivalently corresponds to energetic large scales.

In the particular case of Saffman turbulence ($\sigma = 2$), the value $\alpha_T^\Lambda = 4/5$ was already found by Chasnov (1995). There, the decay and growth laws of passive and active scalar fields, with and without buoyancy or mean gradient, are studied. Power laws for the active scalar field were assessed by large-eddy simulations (LES). Hence, the present EDQNM simulations validate the power laws for the passive scalar field, with an explicit dependence on the initial large-scale conditions σ. Consequently, this analysis can be considered as an extension of Chasnov (1995) regarding the growth of a passive scalar in HITSG.

Then, from the scalar variance evolution equation (4.19), the scalar dissipation should evolve in time similarly as the cospectrum energy,

$$\epsilon_T(t) \sim t^{n_{\epsilon_T}^\Lambda}, \quad n_{\epsilon_T}^\Lambda = \alpha_{\mathscr{F}}, \tag{5.7}$$

in both high- and low-Reynolds-number regimes. This is assessed in figure 12 as well. All the new results regarding the growth or decay predictions for $K_{\mathscr{F}}$, K_T, $\epsilon_{\mathscr{F}}$ and ϵ_T are gathered in table 4.

As a conclusion, the dynamics of a scalar field forced by a mean gradient is fully dominated by the decaying isotropic kinetic field. Indeed, the initial scalar large-scale condition σ_T never appears in the theoretical decay and growth exponents. The velocity field completely leads the dynamics of the flow. This is consistent with a similar result obtained by De Marinis *et al.* (2013) in HIT, where the passive scalar field experiences a Joule heat production. Therefore, it can be concluded that, with a production mechanism, the velocity field completely dominates the passive scalar dynamics.

With these new algebraic exponents for K_T and $K_{\mathscr{F}}$, one can show that for high or low Reynolds numbers, i.e. when both $\alpha_{\mathscr{F}}$ and α_T^Λ are recovered, the correlation $\rho_{w\theta}$ previously investigated is independent of time. Indeed, its algebraic exponent is then

	High-Re regime for all (Λ, σ_T)	Low-Re regime for all (Λ, σ_T)
$K_T(t)$	$\alpha_T^\Lambda = \dfrac{4+p_\mathscr{F}-p}{\sigma-p+3}, p_\mathscr{F} = \begin{cases} 0, & \sigma \leqslant 3 \\ \frac{1}{2}(p+p_T), & \sigma = 4 \end{cases}$	$\alpha_T^\Lambda = -\dfrac{\sigma-3}{2}$
$\epsilon_T(t)$	$n_{\epsilon_T}^\Lambda = \alpha_\mathscr{F} = -\dfrac{\sigma-p_\mathscr{F}-1}{\sigma-p+3}$	$n_{\epsilon_T}^\Lambda = \alpha_\mathscr{F} = -\dfrac{\sigma-1}{2}$
$K_\mathscr{F}(t)$	$\alpha_\mathscr{F} = -\dfrac{\sigma-p_\mathscr{F}-1}{\sigma-p+3}$	$\alpha_\mathscr{F} = -\dfrac{\sigma-1}{2}$
$\epsilon_\mathscr{F}(t)$	Not defined	$n_{\epsilon_\mathscr{F}} = -\dfrac{\sigma+1}{2}$

TABLE 4. Decay and growth exponents of integrated quantities in HITSG for the cospectrum and scalar fields. Here σ is the kinetic infrared slope; p, p_T and $p_\mathscr{F}$ are the backscatter parameters; $\alpha_\mathscr{F}$ and α_T^Λ are the algebraic exponents of the cospectrum energy $K_\mathscr{F}$ and the scalar variance K_T, given in (5.2), (5.3), (5.5) and (5.6); $n_{\epsilon_\mathscr{F}}$ and $n_{\epsilon_T}^\Lambda$ are the algebraic exponents of their corresponding dissipation rates, given in (5.4) and (5.7).

$\alpha_\mathscr{F} - (\alpha + \alpha_T^\Lambda)/2 = 0$. This means that for moderate Reynolds numbers ($Re_\lambda \sim 100$) not high enough to ensure that $\alpha_\mathscr{F}$ and α_T^Λ are verified, $\rho_{w\theta}$ varies in time. This could be the reason for the scattering of the obtained values for $\rho_{w\theta}$ in DNS and experiments, pointed out in § 4.

5.2. *Return to isotropy in HITSG*

The small-scale RTI is briefly investigated for the HITSG configuration, at the level of the scalar second-order moments. Since only the third component of the scalar gradient is non-zero, this is an axisymmetric configuration, meaning that the scalar anisotropy indicators satisfy $2b_{11}^T = 2b_{22}^T = -b_{33}^T$ and $2H_{11}^{(T)} = 2H_{22}^{(T)} = -H_{33}^{(T)}$. In figure 13, the b_{ij}^T are presented: they become constant in both Saffman and Batchelor turbulence, which is qualitatively the same behaviour as the b_{ij} in a sustained shear flow. The spectral anisotropy tensors $H_{ii}^{(T)}$ reveal that small scales of the scalar second-order moments completely return to isotropy for high Reynolds numbers $Re_\lambda \sim 10^3$. Moreover, it has been pointed out in experiments and DNS (Pumir 1994; Danaila *et al.* 1999) that, at the level of the scalar third-order moments, some anisotropy remains in the small scales. This is not incompatible with small-scale isotropic second-order moments, as shown recently by Bos (2014) in HITSG.

5.3. *Growth laws of the energies in HSTSG*

The HSTSG configuration is now considered at very high Reynolds numbers. As mentioned before, the kinetic energy eventually grows exponentially in shear flows at the rate $\gamma = 0.34$, defined in (4.18), within the present anisotropic EDQNM closure in a completely homogeneous framework (Briard *et al.* 2016; Mons *et al.* 2016). In this section, the emphasis is put on the growth of the scalar variance and its interactions with the scalar flux. Some additional results about the passive scalar and the scalar flux are presented, which may be of interest for one-point modelling, such as identifying negligible quantities, and their corresponding mechanisms, at high shear rates.

Firstly, the scalar anisotropy tensors b_{ij}^T are presented in figure 14. As in the HST case without scalar gradient, the scalar indicators reach constant values for large St, and the ratio Λ/S impacts only the short-time dynamics without

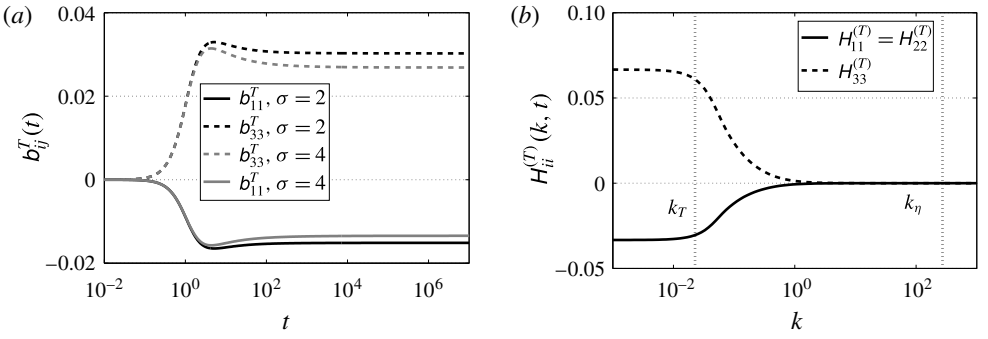

FIGURE 13. (*a*) Diagonal components of b_{ij}^T, defined in (3.5), for both Saffman (black) and Batchelor (grey) turbulence, as a function of time t. (*b*) Diagonal components of $H_{ij}^{(T)}$, defined in (3.3), at $Re_\lambda = 10^3$ for $\sigma = 2$, along with the Kolmogorov and scalar integral wavenumbers k_η and k_T, as a function of the wavenumber k.

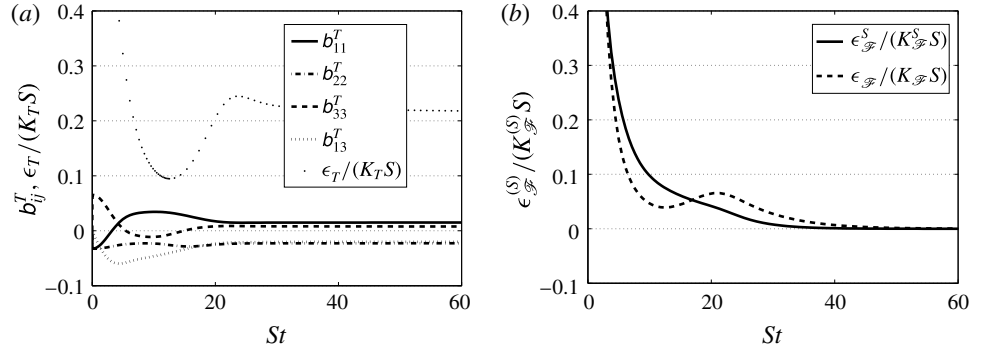

FIGURE 14. Evolution of integrated quantities in HSTSG, as a function of the accumulated anisotropy St, for $\sigma = 2$ and $Re_\lambda(St = 60) = 4 \times 10^4$. (*a*) Scalar anisotropy indicators b_{ij}^T defined in (3.5), and scalar shear rapidity $S_R^T = \epsilon_T/(K_T S)$. (*b*) Ratios $\epsilon_{\mathscr{F}}/(K_{\mathscr{F}} S)$ and $\epsilon_{\mathscr{F}}^S/(K_{\mathscr{F}}^S S)$.

modifying the asymptotic state. There is a noteworthy similarity with the behaviour of $b_{ij} = R_{ij}/(2K) - \delta_{ij}/3$ in shear flows. An interesting feature is that the ratios $\epsilon_{\mathscr{F}}/(K_{\mathscr{F}} S)$ and $\epsilon_{\mathscr{F}}^S/(K_{\mathscr{F}}^S S)$ tend to zero for large St, whereas their kinetic and scalar counterparts do not. This means that the linear effects of shear are preponderant over nonlinear exchanges at the scalar flux level: this is in agreement with figure 8, where the scalar flux transfers of energy are gathered at large scales, dominated by linear mechanisms. The evolution of the scalar, cospectrum and streamwise flux energies are given by

$$\frac{\mathrm{d}K_T}{\mathrm{d}t} = 2\Lambda K_{\mathscr{F}} - \epsilon_T, \tag{5.8}$$

$$\frac{\mathrm{d}K_{\mathscr{F}}}{\mathrm{d}t} = \Lambda R_{33} + \Pi_{\mathscr{F}} - \epsilon_{\mathscr{F}}, \tag{5.9}$$

$$\frac{\mathrm{d}K_{\mathscr{F}}^S}{\mathrm{d}t} = \Lambda R_{13} + SK_{\mathscr{F}} + \Pi_{\mathscr{F}}^S - \epsilon_{\mathscr{F}}^S, \tag{5.10}$$

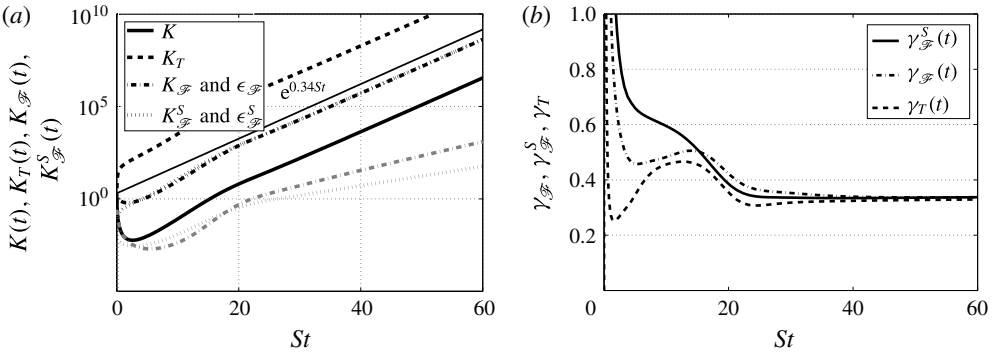

FIGURE 15. Evolution of integrated quantities in HSTSG, as a function of the accumulated anisotropy St, for $\sigma = 2$ and $Re_\lambda(St = 60) = 4 \times 10^4$. (*a*) Exponential growth of the kinetic, scalar, cospectrum and streamwise flux energies. The cospectrum and streamwise flux dissipation rates $\epsilon_{\mathscr{F}}$ and $\epsilon^S_{\mathscr{F}}$ are displayed in grey. (*b*) The exponential growth rates $\gamma_{\mathscr{F}}$, $\gamma^S_{\mathscr{F}}$ and γ_T.

where K_T, $K_{\mathscr{F}}$ and $K^S_{\mathscr{F}}$, respectively, have been defined in (3.6), (4.4) and (4.24). Here is what happens simultaneously: The cross-correlation R_{13} produces $K^S_{\mathscr{F}}$ through the mean scalar gradient Λ. Then R_{13} brings energy to the transverse component R_{33} thanks to nonlinear redistribution, which causes $K_{\mathscr{F}}$ to grow as well through Λ. Finally, $K_{\mathscr{F}}$ provokes the growth of K_T. The main result, displayed in figure 15, is that the scalar variance K_T, which was exponentially decreasing in HST, now grows exponentially in HSTSG. Its scalar growth rate is $\gamma_T = \gamma = 0.34$. This is qualitatively in agreement with the experimental work of Ferchihi & Tavoularis (2002), where the scalar variance and kinetic energy grow exponentially at the same rate in the presence of both mean velocity and scalar gradients. Moreover, both the cospectrum energy $K_{\mathscr{F}}$ and the streamwise flux energy $K^S_{\mathscr{F}}$ grow exponentially with the rate γ as well. This is consistent with the constant scalar flux correlations $\rho_{u_i\theta}$ obtained in § 4 for sufficiently high St. From (5.10), it is possible to determine the analytical expressions of the cospectrum, streamwise flux and scalar exponential growth rates $\gamma_{\mathscr{F}}$, $\gamma^S_{\mathscr{F}}$ and γ_T. Using the fact that $\epsilon_{\mathscr{F}}/(K_{\mathscr{F}}S) \to 0$ and $\epsilon^S_{\mathscr{F}}/(K^S_{\mathscr{F}}S) \to 0$, one has

$$\frac{1}{K_{\mathscr{F}}S}\frac{\mathrm{d}K_{\mathscr{F}}}{\mathrm{d}t} = \underbrace{\frac{\Lambda}{S}\frac{R_{33}}{K_{\mathscr{F}}} + \frac{\Pi_{\mathscr{F}}}{K_{\mathscr{F}}S}}_{\text{constant for } St\gg 1} = \gamma_{\mathscr{F}}, \tag{5.11}$$

$$\frac{1}{K^S_{\mathscr{F}}S}\frac{\mathrm{d}K^S_{\mathscr{F}}}{\mathrm{d}t} = \underbrace{\frac{K_{\mathscr{F}}}{K^S_{\mathscr{F}}}(1+Pr_T) + \frac{\Pi^S_{\mathscr{F}}}{K^S_{\mathscr{F}}S}}_{\text{constant for } St\gg 1} = \gamma^S_{\mathscr{F}}, \tag{5.12}$$

$$\frac{1}{K_TS}\frac{\mathrm{d}K_T}{\mathrm{d}t} = \underbrace{2\frac{\Lambda}{S}\frac{K_{\mathscr{F}}}{K_T} - \frac{\epsilon_T}{K_TS}}_{\text{constant for } St\gg 1} = \gamma_T. \tag{5.13}$$

The agreement between the asymptotic values of these quantities and the value 0.34 expected is presented in figure 15. Moreover, simulations show that $\gamma_{\mathscr{F}}$, $\gamma^S_{\mathscr{F}}$ and γ_T do not depend on large-scale initial conditions σ. All the results regarding the exponential rates of the energies and their dissipation rates in HST and HSTSG are gathered in table 5.

	Exp. rates for all (S, σ, σ_T) in HST	Exp. rates for all (S, Λ, σ) in HSTSG
$K(t)$	$\gamma = 2b_{13} - \dfrac{\epsilon}{KS} = 0.34$	$\gamma = 0.34$
$\epsilon(t)$	γ	γ
$L(t)$	$\dfrac{\gamma}{2}$	$\dfrac{\gamma}{2}$
$K_T(t)$	$\gamma_T = \dfrac{\epsilon_T}{K_T S} = -0.52$	$\gamma_T = \dfrac{2\Lambda K_{\mathscr{F}}}{SK_T} - \dfrac{\epsilon_T}{K_T S} = 0.34$
$\epsilon_T(t)$	γ_T	γ_T
$L_T(t)$	$\dfrac{\gamma}{2}$	$\dfrac{\gamma}{2}$
$K_{\mathscr{F}}(t)$	Not defined	$\gamma_{\mathscr{F}} = \dfrac{\Lambda R_{33}}{SK_{\mathscr{F}}} + \dfrac{\Pi_{\mathscr{F}}}{K_{\mathscr{F}} S} = 0.34$
$K^S_{\mathscr{F}}(t)$	Not defined	$\gamma^S_{\mathscr{F}} = \dfrac{K_{\mathscr{F}}}{K^S_{\mathscr{F}}}(1 + Pr_T) + \dfrac{\Pi^S_{\mathscr{F}}}{K^S_{\mathscr{F}} S} = 0.34$
$\epsilon_{\mathscr{F}}(t)$	Not defined	$\ll \gamma_{\mathscr{F}}$
$\epsilon^S_{\mathscr{F}}(t)$	Not defined	$\ll \gamma^S_{\mathscr{F}}$

TABLE 5. Exponential rates of integrated quantities for the velocity, passive scalar and scalar flux fields in HST and HSTSG: σ and σ_T are the kinetic and scalar infrared slopes; S and Λ are the mean velocity and scalar gradients; and γ, γ_T, $\gamma_{\mathscr{F}}$ and $\gamma^S_{\mathscr{F}}$ are the exponential rates of K, K_T, $K_{\mathscr{F}}$ and $K^S_{\mathscr{F}}$, respectively. The definitions of the kinetic and scalar integrated quantities are recalled in table 3. For the scalar flux: cospectrum energy $K_{\mathscr{F}} = \int \mathscr{F}\,\mathrm{d}k$; streamwise flux energy $K^S_{\mathscr{F}} = \int \mathscr{F}_S\,\mathrm{d}k$; cospectrum energy dissipation rate $\epsilon_{\mathscr{F}} = (\nu + a)\int k^2 \mathscr{F}\,\mathrm{d}k$; and the streamwise flux energy dissipation rate $\epsilon^S_{\mathscr{F}} = (\nu + a)\int k^2 \mathscr{F}_S\,\mathrm{d}k$.

5.4. *Discussion on the streamwise flux spectrum $\mathscr{F}_S(k, t)$ scaling*

The scaling of the streamwise flux $\mathscr{F}_S$ is now addressed. This is of particular interest since $\langle u_1\theta\rangle$ only exists when both mean velocity and scalar gradients are active, such as in atmospheric flows. Wyngaard & Coté (1972) first proposed

$$\mathscr{F}_S(k, t) \sim \Lambda S k^{-3} \tag{5.14}$$

by assuming that $\mathscr{F}_S$ depends on ϵ, k, S and Λ (this expression can also be found starting from $\mathscr{F}_S \sim \Lambda\epsilon^{1/3}k^{-7/3}$ and replacing $\epsilon^{1/3}$ by its expression as a function of the shear scale $\epsilon^{1/3} \sim k^{-2/3}S$). This is not satisfactory, as there is no dependence on ϵ. In a recent paper, Knaus & Pantano (2009) studied reactive and non-reactive scalar flux spectra with DNS and found that a $k^{-7/3}$ range was a satisfactory behaviour. Such a scaling

$$\mathscr{F}_S(k, t) \sim S\epsilon^{-2/3}\epsilon^S_{\mathscr{F}} k^{-7/3} \tag{5.15}$$

assumes that $\epsilon^S_{\mathscr{F}}$ is conserved, which is false, since $\mathscr{F}_S$ is purely anisotropic and does not exist in HIT. With the present modelling, it is revealed in figure 16 that there is a good agreement with the $k^{-23/9}$ scaling predicted by Bos & Bertoglio (2007),

$$\mathscr{F}_S(k, t) = C^S_{\mathscr{F}}\Lambda S^{1/3}\epsilon^{2/9}k^{-23/9}. \tag{5.16}$$

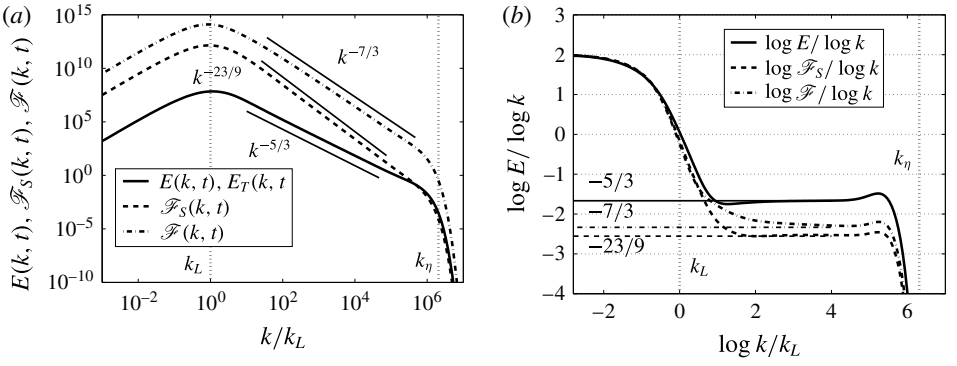

FIGURE 16. (*a*) Kinetic, cospectrum and streamwise flux spectra E, $\mathscr{F}$ and $\mathscr{F}_S$, as a function of the normalized wavenumber k/k_L. (*b*) Associated spectral scaling: the horizontal dashed lines correspond to $-5/3$, $-7/3$ and $-23/9$, as a function of the normalized wavenumber $\log(k/k_L)$. Both at $St = 60$, where $Re_\lambda = 4 \times 10^4$, and $\sigma = 2$.

Numerically, the constant is found to be $C^S_{\mathscr{F}} \simeq 1.5$. This scaling relies on the assumption that one needs to take into account anisotropy for the form of the dissipation rate ϵ. Starting with the scaling of the cospectrum, $\epsilon^{1/3}$ is replaced by $\epsilon_{ij}^{1/3}(k)$, so that

$$F_i(k,t) \sim \lambda_j \epsilon_{ij}^{1/3} k^{-7/3}. \tag{5.17}$$

Then, one has $\epsilon_{ij}(k)E(k) = 3\phi_{ij}(k)\epsilon$, where ϕ_{ij} is the spherical average of the spectral Reynolds tensor. The $k^{-23/9}$ law is recovered using the scaling proposed by Lumley (1967), $\phi_{13} \sim S\epsilon^{1/3}k^{-7/3}$.

5.5. *Return to isotropy in HSTSG*

The small-scale RTI is finally addressed for the HSTSG configuration, at the level of the scalar second-order moments. In figure 17, the scalar anisotropy tensors $H_{ij}^{(T)}$ are presented at large St at two different Reynolds numbers: local isotropy is recovered for the diagonal components of $H_{ij}^{(T)}$, which are zero at small scales, whereas the extra-diagonal component $H_{13}^{(T)}$ shows that some residual anisotropy still remains at small scales. This confirms that, in the presence of shear, and in agreement with most of the DNS and experiments, some anisotropy persists at the scalar small scales, even at the second-order moments level. Furthermore, the Reynolds number is found to have a non-negligible impact on the small-scale anisotropy, as previously noticed by Garg & Warhaft (1998) for the velocity field: indeed, the reduction of small-scale anisotropy, especially for $H_{13}^{(T)}$, is noteworthy from $Re_\lambda = 2400$ (already higher than the Re_λ reached in DNS) to $Re_\lambda = 2 \times 10^4$. The shear wavenumber $k_S = \sqrt{S^3/\epsilon}$ (Corrsin 1958) is displayed as well: for wavenumbers $k > k_S$, nonlinear effects are dominant, consistent with the RTI of small scales, whereas for $k < k_S$, linear effects are stronger and carry most of the anisotropy. A last remark is that the scalar gradient seems to smooth the scalar large-scale anisotropy: indeed, for shear-driven flows without mean scalar gradient, anisotropy is gathered around the scalar peak of energy k_T and is weaker in the infrared range (see figure 6). Whereas for HSTSG, anisotropy progressively increases from moderate to large scales.

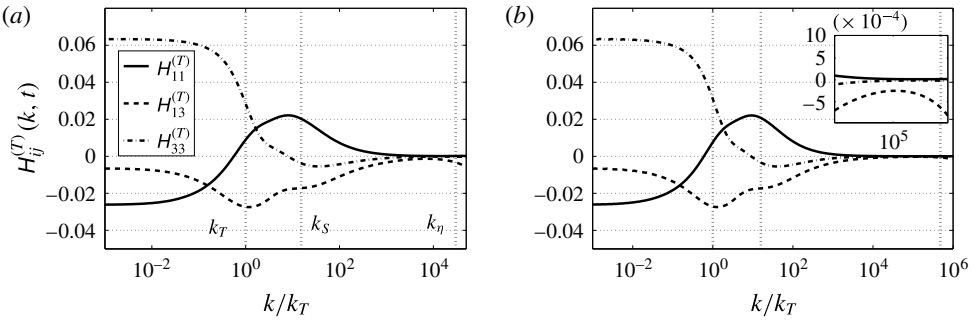

FIGURE 17. Scalar anisotropy descriptors $H_{ij}^{(T)}$, defined in (3.3), along with the Kolmogorov, shear and scalar integral wavenumbers k_η, $k_S = \sqrt{S^3/\epsilon}$ and k_T, for $\sigma = 2$, at two different Reynolds numbers, as a function of the normalized wavenumber k/k_T for: (*a*) $Re_\lambda(St = 40) = 2400$; and (*b*) $Re_\lambda(St = 50) = 2 \times 10^4$. The zoom represents the small scales before k_η where anisotropy persists.

Therefore, the conclusion about the RTI of passive scalar small scales is twofold. Firstly, and consistently with what is observed for shear flows, an increasing Reynolds number is found to reduce small-scale anisotropy for the scalar second-order moments. Nevertheless, some anisotropy remains even at the highest Reynolds numbers reached here ($\sim 10^4$). Secondly, simulations indicate that, at high Reynolds numbers, scalar small scales are still slightly anisotropic in shear-driven flows (with or without an additional mean scalar gradient), whereas they completely return to isotropy when there is only a mean scalar gradient.

6. Conclusion

This study aims at modelling a passive scalar field and its associated scalar flux in homogeneous anisotropic turbulence (HAT). This work is an extension of the modelling developed in Mons *et al.* (2016), which is devoted to the velocity field. A similar two-step approach, which could be called anisotropic EDQNM closure, was consistently applied here. Firstly, dynamical equations that govern the passive scalar and scalar flux fields were closed using a quasi-normal approximation and an isotropic eddy-damping procedure without any assumption regarding anisotropy. Then, for moderately anisotropic flows, scalar spherically averaged descriptors that depend only on the wavenumber modulus k were presented. Consequently, the dynamics of the velocity, passive scalar and scalar flux fields is described by six generalized spherically averaged Lin equations: three for the velocity field, two for the passive scalar and one for the scalar flux. The last three, equations (3.7)–(3.9), represent the first theoretical contribution of this work. These equations are valid for arbitrary mean velocity and scalar gradients of moderate intensity.

Three different homogeneous configurations are considered in this work, whose comprehension is crucial to understand the dynamics of complex flows such as atmospheric ones: isotropic turbulence with a mean scalar gradient (HITSG), shear turbulence (HST) and shear turbulence with a scalar gradient (HSTSG). The anisotropic EDQNM modelling is assessed by detailed comparisons with several DNS and experiments at moderate Reynolds numbers in HITSG and HSTSG: asymptotic values of scalar flux correlations, turbulent Prandtl numbers and diffusivity tensors are well recovered, and the agreement at short time is satisfactory as well.

Then, the model is used to address high-Reynolds-number flows, which are not accessible by DNS yet. In HITSG, the scalar flux along the mean scalar gradient, the cospectrum $\mathscr{F}(k,t)$, is found to scale as $k^{-7/3}$ in the inertial range for very large Reynolds numbers $Re_\lambda \geqslant 10^4$. New results are proposed regarding the decay and growth of $\langle u_3\theta\rangle$ and $\langle\theta\theta\rangle$: theoretical exponents are derived using physical arguments, and are then assessed numerically. Such results have not been provided before and complete the work of Chasnov (1995). This is the second theoretical contribution of this work, which provides further insights into the prediction of high-Reynolds-number decaying turbulence. In HSTSG, the spectral scaling of the streamwise flux $\mathscr{F}_S(k,t)$ in $k^{-23/9}$ is recovered (Bos & Bertoglio 2007), and alternative scalings are briefly discussed. The interesting result of this section is the exponential growth of the passive scalar and scalar flux energies, at a rate equal to that of the kinetic energy. In these three configurations, the small-scale RTI of scalar second-order moments was investigated. Numerical simulations show that scalar small scales return completely to isotropy in HITSG, which is not surprising since the velocity field remains isotropic. On the contrary, when there is a mean velocity gradient (with or without an additional mean scalar gradient), some anisotropy persists in the scalar small scales even at high Reynolds numbers, which is consistent with DNS and experiments. This small-scale anisotropy for the passive scalar is found to diminish with increasing Reynolds number.

Rotation was not investigated in this work, because its effects on triple correlations are not clear, and, as mentioned in the introduction, interacting waves require additional theoretical tools, such as EDQNM2 (Cambon & Jacquin 1989; Sagaut & Cambon 2008), to be properly captured. It is nevertheless a necessary step to the deep understanding of atmospheric flows: the DNS by Brethouwer (2005) suggests that the effects of a rotating shear on the passive scalar transport and its flux are multiple and rather complex. Finally, the present modelling could be easily applied to unstably stratified homogeneous turbulence (USHT), since stratification amounts only to additional linear transfers, much simpler than the ones induced by mean-velocity gradients. USHT was recently investigated by Burlot *et al.* (2015) with a different anisotropic EDQNM approach, without reduction in terms of spherically averaged descriptors: the linear parts (of the $\boldsymbol{k}$-dependent Craya equations) are exactly computed, but the numerical integration of the nonlinear transfers requires huge computational resources.

In conclusion, this anisotropic EDQNM modelling seems promising since it recovers quite well previous experimental and numerical results, and additionally permits one to explore large Reynolds numbers. It can predict the velocity and scalar field dynamics for various kinds of anisotropy with the same consistent method and does not rely on adjustable constants, except the classical ones used in the eddy-damping factors. The objective of this ongoing work is to provide a complete mapping of the scalar field in HAT with three parameters: the shear rate S, the scalar gradient Λ, and the Prandtl number Pr, whose effects on the passive scalar dynamics will be the subject of a subsequent study.

Acknowledgements

The authors are grateful to V. Mons for valuable discussions.

Appendix A. Scalar infrared slope

In this appendix, some details are given to explain why there is no loss of generality when the infrared kinetic and scalar slopes σ and σ_T are chosen to be

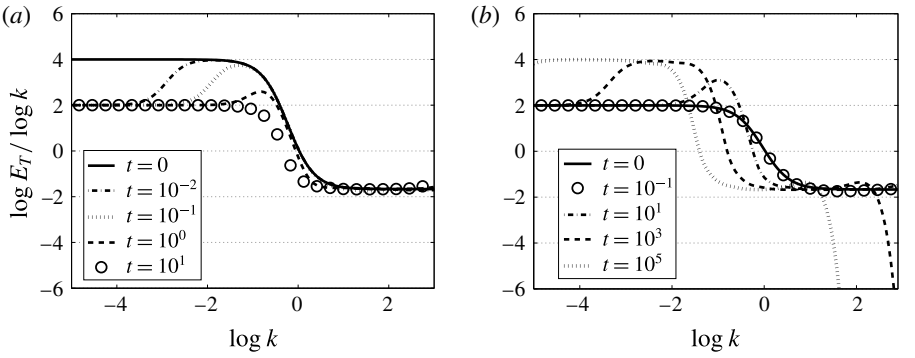

FIGURE 18. Spectral evolution of the scalar infrared slope σ_T for $Re_\lambda(0) \sim 3 \times 10^3$, as a function of the wavenumber $\log k$ for: (*a*) $\sigma_T(t=0) = 4$ and $\sigma = 2$; and (*b*) $\sigma_T(t=0) = 2$ and $\sigma = 4$.

equal. The scalar gradient Λ results in a production term in the passive scalar equation. This scalar production is linked to the cospectrum, itself linked to the kinetic energy spectrum. Hence, the 'minimum of energy' of the flow is imposed by the infrared range of the kinetic spectrum (i.e. imposed by σ). So, the scalar infrared exponent σ_T changes if initially different from σ.

For instance, if $\sigma_T(t=0) > \sigma$, this rapidly results in $\sigma_T = \sigma$. Indeed, $\sigma_T > \sigma$ means $K_T < K$: as the kinetic field imposes the minimum of energy, σ_T will decrease down to σ. For instance, if one has $\sigma_T(t=0) = 4$ and $\sigma = 2$, the self-similar regime is $\sigma = \sigma_T = 2$ (and so for this flow $p_T = 0$).

Similarly, if $\sigma_T < \sigma$, then $\sigma_T = \sigma$ but it takes more time, as revealed in figure 18. Once again, this is because of the velocity field. Without the scalar gradient, the scalar variance would decrease more slowly than the kinetic energy. The production term being proportional to $K(t)$, it forces the scalar field to grow with the infrared slope $\sigma_T = \sigma$.

Appendix B. Additional comparison

Here, for historical reasons, simulations are compared to the experiment of Tavoularis & Corrsin (1981), which was one of the first experiments to deeply investigate the HSTSG configuration. The mean speed is $U_c = 12.4$ m s^{-1} and the characteristic length is the shear generator one $h = 0.305$ m. The velocity gradient is $\mathrm{d}U_1/\mathrm{d}x_2 = 46.8$ m s^{-1} and the scalar one $\mathrm{d}T/\mathrm{d}x_2 = 9.5\,^{\circ}$C m^{-1}. From the data of the kinetic characteristic time written $\tau_u = 2\tau_0 = 0.26$ s, $S = 6.19\tau_0^{-1}$ is found. Then, from the scalar characteristic time τ_θ and the mean scalar fluctuations $\langle\theta^2\rangle$, it is possible to compute the reference scalar gradient. Let us mention that initial isotropic conditions are used, which is clearly not the case in the experiment. Two final Reynolds numbers are proposed: $R_{\lambda_g} = 160$ scaled for isotropic turbulence, and $R_{\lambda_{11}} = 266$ for inhomogeneous flows, chosen here as it appears to be more appropriate.

The comparisons are presented in figure 19. Data are available at three locations: $x_1/h = 7.5$, 9.5 and 11. Using the appropriate conversion in dimensionless time $St = (x_1/U_c)(\mathrm{d}U_1/\mathrm{d}x_2)$, this provides experimental information at $St = 8.63$, 10.94 and 12.66. There are good agreements in figure 19 for the cospectrum and streamwise flux correlations $\rho_{v\theta}$ and $\rho_{u\theta}$. Similar values for $\rho_{u\theta}$ and $\rho_{v\theta}$ are reported in Ferchihi & Tavoularis (2002). There is a satisfactory agreement as well for the

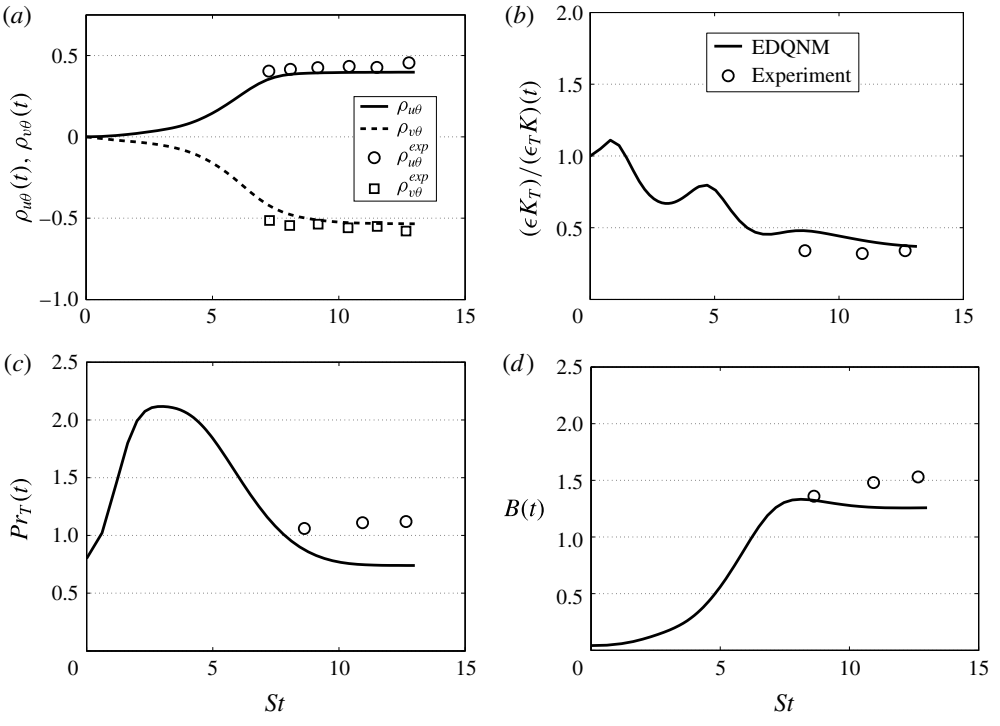

FIGURE 19. Comparisons with the experimental results of Tavoularis & Corrsin (1981), for $\sigma = 2$, $S = 6.19\tau_0^{-1}$ and $\mathscr{S}_\theta = 0.1823$, as a function of the accumulated anisotropy St. (a) The scalar flux correlations $\rho_{u_i\theta}$ defined in (4.15). (b) The inverse of the time-scale ratio defined in (4.16). (c) The turbulent Prandtl number Pr_T defined in (4.26). (d) The relative strength of the fluctuations $B = \sqrt{3}/\beta$ where β is defined in (4.27).

characteristic times ratio $\tau_\theta/\tau_u = 1/R_T$, where R_T has been defined in (4.16). A first discrepancy is observed for $B(t) = \sqrt{3}/\beta$, where β has been defined in (4.27), which is underestimated in the present simulations. Let us point out that all measured quantities except $B(t)$ have converged, which is not realistic. Moreover, $B(t)$ seems to be very dependent on the initial conditions, which could explain the present difference. One has to keep in mind that the initial condition is isotropic, whereas in the experiment there is initially anisotropy in the flow, which is difficult to model. This may explain as well the strong variations observed for $(\epsilon K_T)/(\epsilon_T K)$ at small St. Finally, a difference is observed for the turbulent Prandtl number, defined in (4.26), which is here $Pr_T = (\Lambda/S)(R_{12}/K_{\mathscr{F}})$. The value obtained experimentally, $Pr_T^{exp} \simeq 1.1$, seems quite large compared to the EDQNM value, $Pr_T^{EDQNM} \simeq 0.74$. Indeed, Herring *et al.* (1982) and Lesieur (2008) have both reported, from atmospheric data and theoretical considerations, that one should obtain $0.6 \leqslant Pr_T \leqslant 0.8$, which is in agreement with the present results. Moreover, other values of the turbulent Prandtl numbers reported from DNS and experiments agree better with 0.7 than with 1.1 (Shirani *et al.* 1981; Rogers *et al.* 1989). Let us mention that the comparison with Bos & Bertoglio (2007) for Pr_T is not relevant because a constant of their model for linear transfers is set so that $Pr_T^{exp} = 1.1$ is recovered.

REFERENCES

BOS, W. J. T. 2014 On the anisotropy of the turbulent passive scalar in the presence of a mean scalar gradient. *J. Fluid Mech.* **744**, 38–64.

BOS, W. J. T. & BERTOGLIO, J.-P. 2007 Inertial range scaling of scalar flux spectra in uniformly sheared turbulence. *Phys. Fluids* **19**, 025104.

BOS, W. J. T., TOUIL, H. & BERTOGLIO, J.-P. 2005 Reynolds number dependency of the scalar flux spectrum in isotropic turbulence with a uniform scalar gradient. *Phys. Fluids* **17**, 125108.

BOS, W. J. T., TOUIL, H., SHAO, L. & BERTOGLIO, J.-P. 2004 On the behavior of the velocity–scalar cross correlation spectrum in the inertial range. *Phys. Fluids* **16**, 3818.

BRETHOUWER, G. 2005 The effect of rotation on rapidly sheared homogeneous turbulence and passive scalar transport. Linear theory and direct numerical simulation. *J. Fluid Mech.* **542**, 305–342.

BRIARD, A., GOMEZ, T., MONS, V. & SAGAUT, P. 2016 Decay and growth laws in homogeneous shear turbulence. *J. Turbul.* **17** (7), 699–726.

BRIARD, A., GOMEZ, T., SAGAUT, P. & MEMARI, S. 2015 Passive scalar decay laws in isotropic turbulence: Prandtl number effects. *J. Fluid Mech.* **784**, 274–303.

BURLOT, A., GRÉA, B.-J., GODEFERD, F. S., CAMBON, C. & GRIFFOND, J. 2015 Spectral modelling of high Reynolds number unstably stratified homogeneous turbulence. *J. Fluid Mech.* **765**, 17–44.

CAMBON, C. & JACQUIN, L. 1989 Spectral approach to non-isotropic turbulence subjected to rotation. *J. Fluid Mech.* **202**, 295–317.

CAMBON, C., JEANDEL, J. & MATHIEU, J. 1981 Spectral modelling of homogeneous non-isotropic turbulence. *J. Fluid Mech.* **104**, 247–262.

CAMBON, C. & RUBINSTEIN, R. 2006 Anisotropic developments for homogeneous shear flows. *Phys. Fluids* **18**.

CHASNOV, J. R. 1995 Similarity states of passive scalar transport in buoyancy-generated turbulence. *Phys. Fluids* **7** (6), 1498–1506.

COMTE-BELLOT, G. & CORRSIN, S. 1966 The use of a contraction to improve the isotropy of a grid generated turbulence. *J. Fluid Mech.* **25**, 657–682.

CORRSIN, S. 1958 On local isotropy in turbulent shear flow. *NACA RM* 58B11.

DANAILA, L., LE GAL, P., ANSELMET, F., PLAZA, F. & PINTON, J. F. 1999 Some new features of the passive scalar mixing in a turbulent flow. *Phys. Fluids* **11**, 636–646.

DE MARINIS, D., CHIBBARO, S., MELDI, M. & SAGAUT, P. 2013 Temperature dynamics in decaying isotropic turbulence with Joule heat production. *J. Fluid Mech.* **724**, 425–449.

DE SOUZA, F. A., NGUYEN, V. D. & TAVOULARIS, S. 1995 The structure of highly sheared turbulence. *J. Fluid Mech.* **303**, 155–167.

FERCHIHI, M. & TAVOULARIS, S. 2002 Scalar probability density function and fine structure in uniformly sheared turbulence. *J. Fluid Mech.* **461**, 155–182.

GARG, S. & WARHAFT, Z. 1998 On the small scale structure of simple shear flow. *Phys. Fluids* **10**, 662–673.

GOMEZ, T., POLITANO, H. & POUQUET, A. 2000 Exact relationship for third-order structure functions in helical flows. *Phys. Rev.* E **61** (5), 5321–5325.

GONZALEZ, M. 2000 Asymptotic evolution of a passive scalar advected by homogeneous turbulent shear flow. *Intl J. Heat Mass Transfer* **43**, 387–397.

GYLFASON, A. & WARHAFT, Z. 2009 Effects of axisymmetric strain on a passive scalar field: modelling and experiment. *J. Fluid Mech.* **628**, 339–356.

HERR, S., WANG, L.-P. & COLLINS, L. R. 1996 EDQNM model of a passive scalar with a uniform mean gradient. *Phys. Fluids* **8**, 1588.

HERRING, J. R., SCHERTZER, D., LESIEUR, M., NEWMAN, G. R., CHOLLET, J. P. & LARCHEVEQUE, M. 1982 A comparative assessment of spectral closures as applied to passive scalar diffusion. *J. Fluid Mech.* **124**, 411–437.

JAYESH & WARHAFT, Z. 1992 Probability distribution, conditional dissipation, and transport of passive temperature fluctuations in grid-generated turbulence. *Phys. Fluids* A **4**.

KADER, B. A. & YAGLOM, A. M. 1991 Spectra and correlation functions of surface layer atmospheric turbulence in unstable thermal stratification. In *Fluid Mechanics and its Applications* (ed. O. Metais & M. Lesieur), pp. 387–412. Springer.

KARNIK, U. & TAVOULARIS, S. 1989 Measurements of heat diffusion from a continuous line source in a uniformly sheared turbulent flow. *J. Fluid Mech.* **202**, 233–261.

KASSINOS, S. C., KNAEPEN, B. & CARATI, D. 2007 The transport of a passive scalar in magnetohydrodynamic turbulence subjected to mean shear and frame rotation. *Phys. Fluids* **19**, 015105.

KNAUS, R. & PANTANO, C. 2009 On the effect of heat release in turbulence spectra of non-premixed reacting shear layers. *J. Fluid Mech.* **626**, 67–109.

KOLMOGOROV, A. N. 1941 The local structure of turbulence in incompressible viscous fluid for very large Reynolds numbers. *Dokl. Akad. Nauk SSSR* **30** (301).

LEITH, C. E. 1971 Atmospheric predictability and two-dimensional turbulence. *J. Atmos. Sci.* **28**, 145–161.

LESIEUR, M. 2008 *Turbulence in Fluids*, 4th edn. Springer.

LUMLEY, J. L. 1967 Similarity and the turbulent energy spectrum. *Phys. Fluids* **10** (4), 855–858.

MEYERS, J. & MENEVEAU, C. 2008 A functional form of the energy spectrum parametrizing bottleneck and intermittency effects. *Phys. Fluids* **20**, 065109.

MONS, V., CAMBON, C. & SAGAUT, P. 2016 A spectral model for homogeneous shear-driven anisotropic turbulence in terms of spherically-averaged descriptors. *J. Fluid Mech.* **788**, 147–182.

MYDLARSKI, L. 2003 Mixed velocity–passive scalar statistics in high-Reynolds-number turbulence. *J. Fluid Mech.* **475**, 173–203.

MYDLARSKI, L. & WARHAFT, Z. 1998 Passive scalar statistics in high-Péclet-number grid turbulence. *J. Fluid Mech.* **358**, 135–175.

O'GORMAN, P. A. & PULLIN, D. I. 2003 The velocity–scalar cross spectrum of stretched spiral vortices. *Phys. Fluids* **15**, 280.

O'GORMAN, P. A. & PULLIN, D. I. 2005 Effect of Schmidt number on the velocity scalar cospectrum in isotropic turbulence with a mean scalar gradient. *J. Fluid Mech.* **532**, 111–140.

ORSZAG, S. A. 1970 Analytical theories of turbulence. *J. Fluid Mech.* **41**, 363–386.

ORSZAG, S. A. 1977 The statistical theory of turbulence. In *Fluid Dynamics* (ed. A. Balian & J. L. Peube), pp. 237–374. Gordon and Breach.

OVERHOLT, M. R. & POPE, S. B. 1996 Direct numerical simulation of a passive scalar with imposed mean gradient in isotropic turbulence. *Phys. Fluids* **8** (11), 3128–3148.

POPE, S. B. 2000 *Turbulent Flows*. Cambridge University Press.

POUQUET, A., LESIEUR, M., ANDRE, J. C. & BASDEVANT, C. 1975 Evolution of high Reynolds number two-dimensional turbulence. *J. Fluid Mech.* **72**, 305–319.

PUMIR, A. 1994 A numerical study of the mixing of a passive scalar in three dimensions in the presence of a mean gradient. *Phys. Fluids* **6** (6), 2118–2132.

PUMIR, A. 1996 Turbulence in homogeneous shear flows. *Phys. Fluids* **8** (11), 3112–3127.

ROGERS, M. M., MANSOUR, N. N. & REYNOLDS, W. C. 1989 An algebraic model for the turbulent flux of a passive scalar. *J. Fluid Mech.* **203**, 77–101.

SAGAUT, P. & CAMBON, C. 2008 *Homogeneous Turbulence Dynamics*. Cambridge University Press.

SHEN, X. & WARHAFT, Z. 2000 The anisotropy of the small scale structure in high Reynolds number ($r_\lambda \sim 1000$) turbulent shear flow. *Phys. Fluids* **12** (11), 2976–2989.

SHIRANI, E., FERZIGER, J. H. & REYNOLDS, W. C. (1981) Mixing of a passive scalar in isotropic and sheared homogeneous turbulence. *NASA Rep. No.* Tf-15 NASA-CR-164938.

SIRIVAT, A. & WARHAFT, Z. 1983 The effect of a passive cross-stream temperature gradient on the evolution of temperature variance and heat flux in grid turbulence. *J. Fluid Mech.* **128**, 323–346.

SPEZIALE, C. G., SARKAR, S. & GATSKI, T. B. (1990) Modeling the pressure–strain correlation of turbulence – an invariant dynamical systems approach. *NASA Contractor Rep.* 181979.

SREENIVASAN, K. R. 1991 On local isotropy of passive scalars in turbulent shear flows. *Proc. Math. Phys. Sci.* **434**, 165–182.

SREENIVASAN, K. R., ANTONIA, R. A. & BRITZ, D. 1979 Local isotropy and large structures in a heated turbulent jet. *J. Fluid Mech.* **94**, 745–775.

SREENIVASAN, K. R. & TAVOULARIS, S. 1980 On the skewness of the temperature derivative in turbulent flows. *J. Fluid Mech.* **101**, 783–795.

TAVOULARIS, S. & CORRSIN, S. 1981 Experiments in nearly homogenous turbulent shear flow with a uniform mean temperature gradient. Part 1. *J. Fluid Mech.* **104**, 311–347.

VENKATARAMANI, K. S. & CHEVRAY, R. 1978 Statistical features of heat transfer in grid-generated turbulence: constant-gradient case. *J. Fluid Mech.* **86**, 513–543.

WALEFFE, F. 1992 The nature of triad interactions in homogeneous turbulence. *Phys. Fluids* **4**, 350–363.

WARHAFT, Z. 1980 An experimental study of the effect of uniform strain on thermal fluctuations in grid-generated turbulence. *J. Fluid Mech.* **99**, 545–573.

WATANABE, T. & GOTOH, T. 2007 Scalar flux spectrum in isotropic steady turbulence with a uniform mean gradient. *Phys. Fluids* **19**.

WYNGAARD, J. C. & COTÉ, O. R. 1972 Cospectral similarity in the atmospheric surface layer. *Q. J. R. Meteorol. Soc.* **98**, 590–603.